

3D photophoretic aircraft made from ultralight porous materials can carry kg-scale payloads in the mesosphere

Thomas Celenza, Andy Eskenazi and Igor Bargatin

We show that photophoretic aircraft would greatly benefit from a three-dimensional (3D) hollow geometry that pumps ambient air through sidewalls to create a high-speed jet. To identify optimal geometries, we developed a theoretical expression for the lift force based on both Stokes (low-Re) and momentum (high-Re) theory and validated it using finite-element fluid-dynamics simulations. We then systematically varied geometric parameters, including Knudsen pump porosity, to minimize the operating altitude or maximize the payload. Assuming that the large vehicles can be made from previously demonstrated nanocardboard material, the minimum altitude is 55 km while the payload can reach 1 kilogram for 3D structures with 10-meter diameter at 80 km altitude. In all cases, the maximum areal density of the sidewalls cannot exceed a few grams per square meter, demonstrating the need for ultralight porous materials.

For centuries, humans have been exploring Earth's atmosphere and outer space, a quest that has led to discoveries in fields ranging from aerodynamics to astronomy and climate modeling [1-3]. However, the study of certain regions of the atmosphere is hindered by available propulsion technologies. For instance, in Earth's mesosphere, anthropogenic emissions of carbon dioxide are counterintuitively producing rapid cooling [4]. The shrinking of the atmosphere resulting from this cooling [5] can be problematic, given that a contracting mesosphere can result in reduced satellite drag, which could translate into a greater accumulation of space debris [6]. Unfortunately, uncertainties in calculations of these effects are currently large because experimental observations within the mesosphere are challenging [7], given that this region, extending from fifty to eighty kilometers above the surface of Earth, has air pressures too low to sustain planes or balloons and too high for orbiting satellites.

Another region of significant interest is the Martian atmosphere, where most recently the helicopter Ingenuity achieved near-surface flight [8]. Even with this milestone, sustained flight at high altitudes in Mars, e.g., from Olympus Mons, is not yet possible due to decreasing atmospheric density [9,10]. Like the study of Earth's mesosphere, the exploration of Mars' atmosphere at high altitudes is limited by the lack of long-duration methods of flight and propulsion at ambient pressures below ~ 1 mbar (100 Pa). As a result, developing an airborne platform that can operate in a very thin atmosphere, both on Mars and on Earth, would be extremely useful in helping collect valuable and atmospheric data related to wind patterns, temperature and pressure variations, as well as the concentrations of atmospheric gases.

One promising concept, based on the lightweight light-powered centimeter-scale microflyers developed by Cortes *et al.* [11], can potentially overcome the issues faced by the current propulsion mechanisms and achieve sustained flight in Earth's mesosphere and the Martian atmosphere. These devices, composed of porous plates, can levitate due to photophoresis, a light-driven propulsion mechanism where a jet is created using Knudsen pumping of ambient gas [12]. Knudsen pumps have no moving parts and instead exploit temperature gradients to induce gas flows through these plates. Known as "nanocardboard", these ultralight porous plates are composed of nanometer-thick (25–400 nm) aluminum oxide face sheets that are connected by channels with micrometer-scale width and height. They offer an areal density of only ~ 1 g/m² and a bending stiffness orders of magnitude higher relative to solid plates of the same mass [13].

Photophoretic levitation is typically enabled by a difference in physical properties between the top and bottom of the plate. For instance, in the study performed by Cortes *et al.* [12], the bottom side of the nanocardboard was coated with carbon nanotubes (CNTs), which absorbed the incident light and subsequently increased in temperature relative to the top side. This difference in temperatures caused the Knudsen pumping, which pushed air down through the channels of nanocardboard from the cold to the hot side and thus creating a downward jet below the nanocardboard that levitated plates with centimeter-scale sizes [11]. This mechanism works best in low pressure environments (1-100 Pa) [14], such as in Earth's mesosphere or near the top of Olympus Mons on Mars [15]. If the lift forces are large enough to carry tiny "smart dust" sensor payloads [16], many such microflyers can be deployed on Earth or on Mars to record data in these regions of the atmosphere.

In this work, we propose much larger photophoretic vehicles, which are many meters in diameter, three-dimensional rather than planar, and use porous sidewalls that push air into an inner chamber and out

of a small nozzle (**Fig. 1**). Using the nozzle increases the speed of the air jet, and such 3D photophoretic vehicles can not only increase the resulting lift force but also widen the range of operating pressures. Combining design concepts from the previously demonstrated photophoretic levitation of planar nanocardboard [11] and analytical tools we used for solid mylar-CNT composite disks [17], we analyzed 3D geometries with porous alumina nanocardboard walls and CNTs deposited on their inner side. Because alumina is transparent, CNTs on the inside of the structure would absorb the incident light, inducing the Knudsen pumping of air from the outside into the interior chamber through the pores and then out of the chamber through the exit nozzle, producing a jet as illustrated in **Fig. 1**.

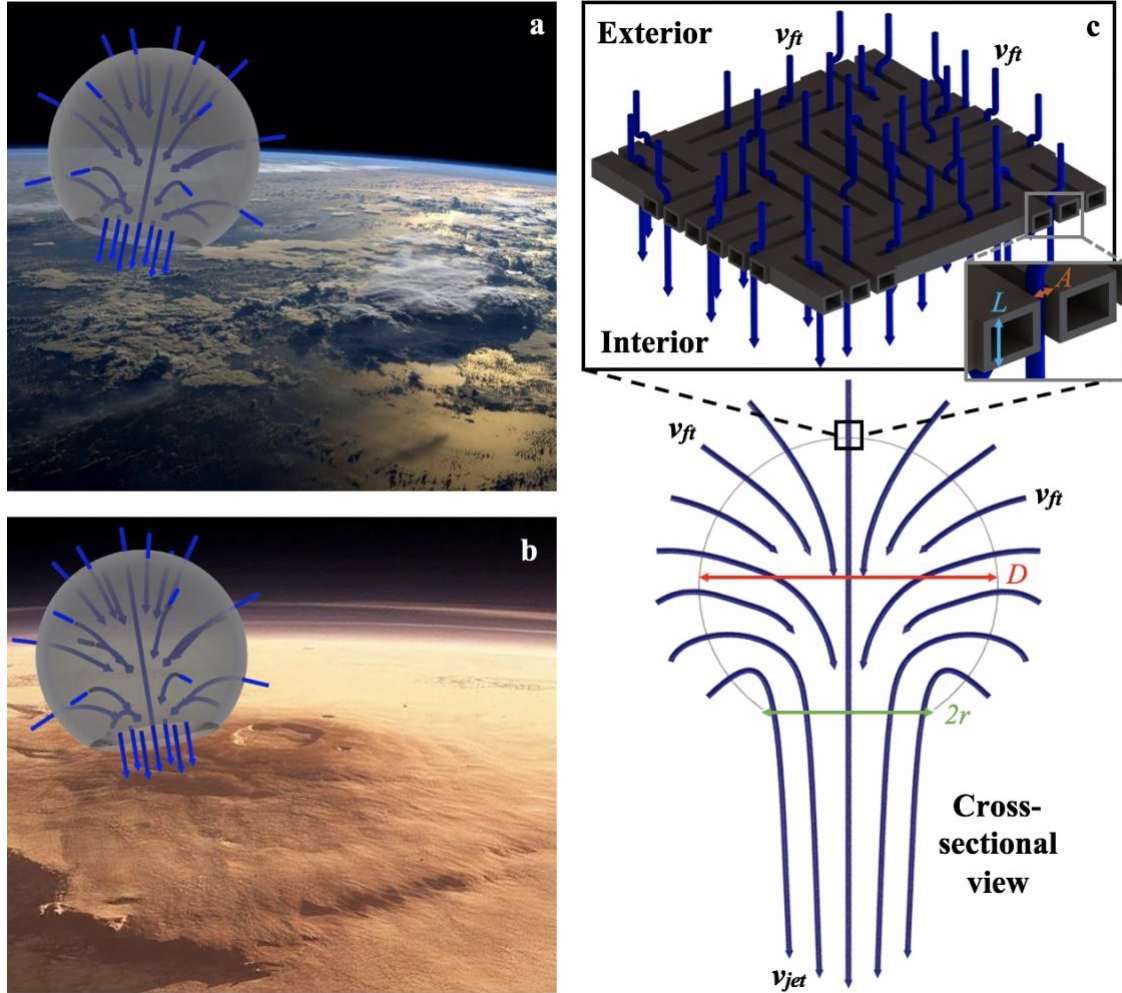


Figure 1: A hollow sphere with porous alumina-CNT composite walls flying in Earth's mesosphere (a) and over the top of Olympus Mons in Mars (b). The cross-sectional view (c) of the sphere shows the air flow in, with velocity v_{ft} , due to Knudsen pumping (across the nanocardboard walls, as seen on the zoomed-in view) and out as a jet through the exit nozzle, with velocity v_{jet} . As depicted in (c), A is the nanocardboard channel width, L the nanocardboard channel height, and r the structure's outlet radius, while D the structure's overall size dimension. Background Earth and Mars Image Credits: NASA.

To identify the optimal 3D geometry that maximized payload, we considered three representative geometries (a sphere, a cone, and a rocket), and performed a series of simulations to determine the parameters that would yield the greatest lift forces. However, first, it was necessary to develop an analytical expression that predicted the lift forces produced by such structures across a wide range of Reynold numbers. To determine this expression, we modeled these 3D structures with outlet jet velocities as small as 10^{-6} m/s to as large as ~ 100 m/s and at various atmospheric altitudes up to 80 km using computational fluid dynamics simulations in ANSYS Fluent, as detailed in the supplementary information. For each fluid-flow simulation, we found the reaction forces induced from the air flow (equal and opposite to the lift force), and then fitted the collected data using the equation

$$F = C_1 8\mu D v_{ft} + C_2 \rho A v_{jet}^2. \quad (1)$$

Here, μ corresponded to the fluid viscosity, ρ to the density, $A = \pi r^2$ is the area of a nozzle with radius r , D is the geometry’s characteristic (i.e., largest) dimension, while v_{ft} is the flow-through velocity of the fluid flow through the porous material and v_{jet} is the velocity of the fluid exiting the structure through the small nozzle. As outlined in the supplementary information, v_{ft} depends on the light intensity, I , the altitude dependent air pressure, P , and the geometric parameters of the nanocardboard. The upper limit of the flow-through velocity typically scales as $v_{ft} \approx 0.03 I/P$ (see supplementary information), resulting in velocities of less than 1 mm/s under natural sunlight ($\sim 1000 \text{ W/m}^2$) and standard atmospheric pressure (10^5 Pa) but increasing by many orders of magnitude as the pressure drops at higher altitudes.

In Eqn. (1), the first term is based on Stokes’ drag on a disk, obtained from a linearization of the steady-state Navier-Stokes equations in the case of dominating viscous forces, i.e., in the low-Re limit. Cortes *et al.* previously showed that at vanishingly low air flow speeds, the lift of a stationary nanocardboard plate with air flowing through it was equal to the Stokes drag for a solid disk [11]. In contrast, at high jet speeds, the inertial terms dominate, and the lift is mostly dependent on the velocity of the jet exiting the nozzle. The helicopter-momentum theory equation, which can be derived from a simple application of Reynolds Transport Theorem and represents the second term in Eqn. (1), can model the lift in this high-Re limit. Summing both terms results in a simple interpolation between the two operating regimes that gives an estimate for the lift force at all pressures and velocities (and, therefore, all values of Re). **Table 1** summarizes the average fitted C_1 and C_2 parameters, both on the order of 1, obtained from fitting the results for 27 ANSYS Fluent simulations using 3 different altitudes (0 km, 40 km and 70 km), 3 geometry types (sphere, cone, and rocket), and 3 different structure sizes (1cm, 5cm and 10cm).

Fitting Parameters for Each Geometry			
Geometry	Cone	Sphere	Rocket
C_1	1.2	1.3	1.4
C_2	0.9	0.9	0.4

Table 1: Fitting parameters for the three geometries in addition to key dimensions. Notice that these ANSYS simulations were performed assuming a 100% porosity along each one of these structures’ walls.

After determining the coefficients C_1 and C_2 , we proceeded to numerically optimize the various parameters controlling the overall 3D shape and nanocardboard porous microstructure to maximize the payload capabilities. The developed MATLAB code [18] was based on the photophoretic levitation theory for nanocardboard [11] adapted to axisymmetric 3D structures, as detailed in the supplementary information. The code also took into account how temperature and pressure depend on the altitude in the atmosphere, employing empirical relations developed from standard atmospheric data [19]. Our optimization sought the combination of A (nanocardboard channel width), L (nanocardboard channel height), and r (the structure’s outlet/nozzle radius) that resulted in the highest payload or achieved flight at the lowest altitude as a function of the overall aircraft size D (diameter for sphere and cone, and length for the rocket). All these geometric parameters are illustrated in **Fig. 1c**.

Our numerical optimizations revealed that the optimal nanocardboard porosity parameters A and L were of the same order of magnitude across all geometries and dimensions D . When optimized for achieving flight at the minimum altitude (55 km with zero-payload), A and L were $\approx 0.20 \text{ mm}$ and $\approx 0.21 \text{ mm}$, respectively. When optimized for maximum payload (achieved at 80 km altitude), A and L were 0.90 mm and 0.91 mm, or about a factor of 4 greater. Because these parameters are of the same order of magnitude despite the approximately 40-fold change in ambient pressure at the minimum possible altitude of 55 km and the max payload altitude of 80 km, we can make structures that simultaneously achieve levitation at low altitudes while carrying significant payload at higher altitudes.

The maximum areal densities, i.e., the maximum lift force divided by specific gravity g and the area of nanocardboard, were also comparable for all structures. **Table 2** shows that the typical value of maximum areal density was $\approx 7.1 \text{ g/m}^2$ (grams per square meter) for small aircraft ($D = 10 \text{ cm}$) compared to $\approx 5.5 \text{ g/m}^2$ for large aircraft ($D = 10 \text{ m}$). Both these densities are in the same order of magnitude as the theoretical upper limit derived for the high-Re case in the supplementary information, of $0.016 I / (v_{avg} g) \approx 0.004 \text{ kg/m}^2 = 4 \text{ g/m}^2$. Here, $v_{avg} = \sqrt{8R_{air}T/\pi} \approx 400 \text{ m/s}$ is average speed of air molecules at 55-80 km altitudes, while $R_{air} = R_u/M_{air} = 287 \text{ J}/(\text{kg} \cdot \text{K})$ is the gas-specific ideal constant of air, equal to the universal gas constant R_u divided by the average molar mass of air M_{air} . **Fig 2a** shows how the maximum areal densities varies with aircraft size D and, therefore, the airflow’s Reynolds number.

The permissible areal densities of each structure decrease with increasing size and Re and stabilize at ~ 5.5 g/m² for larger aircraft that carry payloads of 1 gram or more.

Areal Densities and Areas Ratio							
Geometry		Cone		Sphere		Rocket	
		D = 10 cm	D = 10 m	D = 10 cm	D = 10 m	D = 10 cm	D = 10 m
Max Areal Density	For Max. Payload	6.6 g/m ²	5.4 g/m ²	7.8 g/m ²	5.5 g/m ²	6.9 g/m ²	5.7 g/m ²
Area Ratios	For Min. Altitude	18	26	26	27	23	25
	For Max. Payload	5	5	5	6	6	6

Table 2: Summary of the parametric studies results for the Cone, Sphere and Rocket, for values of $D = 10$ cm and $D = 10$ m (full data for all the probed values of D can be found in the supplementary information section). Here, the area ratio refers to the A_{total}/A_{out} ratio, of the structure's total surface area to its outlet area.

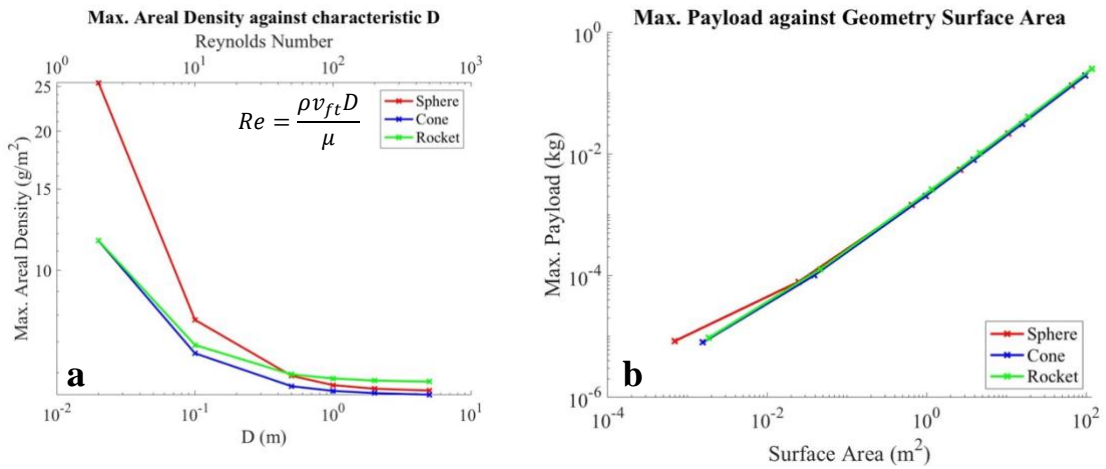


Figure 2: Areal Density versus Characteristic Size (a) and Maximum Payload versus Surface Area (b) for the three considered 3D geometries at 80-km altitude. Each data point corresponds to the optimized geometry at each of the probed values of the parameter D . The overlap between the curves, in particular starting at surface areas larger than 0.01 m², suggests that the geometries have similar areal densities and maximum payload capabilities.

Plotting maximum payloads against the structure surface area in **Fig. 2b** revealed that, for a given surface area, the maximum payload was very similar across all three geometries. While the sphere outperformed at smallest sizes, all three shapes (cone, sphere, and rocket) offered essentially the same performance at the largest sizes, i.e., for sizes that maximize the payload and are most promising for practical applications. **Fig. 3** below illustrates optimized shapes for the 10-meter cone (a), sphere (b) and rocket (c), which could carry 780, 540, and 1020 grams of payload, respectively. This is sufficient capacity to carry modern communication devices [20] and similar to the payload of a typical CubeSat [21].

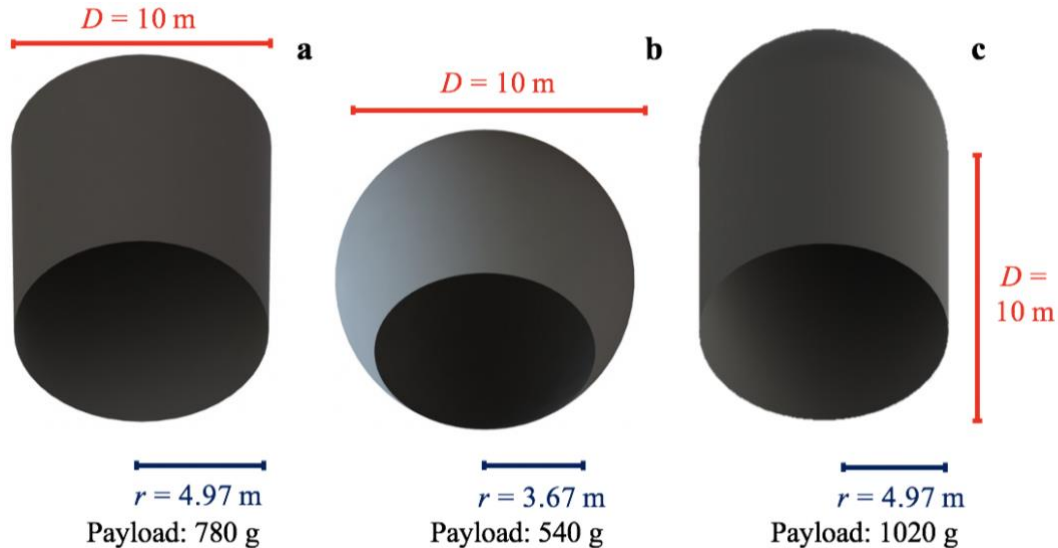


Figure 3: Geometrically optimized cone (a), sphere (b) and rocket (c) for maximum payload capabilities with a fixed characteristic dimension of $D = 10$ meters. D represents the cone and sphere diameter, and the rocket length. Achieving a payload of 1kg required a D of 11.5 and 14 m for the cone and sphere, respectively.

Finally, as demonstrated in **Table 2** and the supplementary information section, we noticed that the A_{total}/A_{out} ratio, of the total surface area to the outlet area, was approximately constant for the optimal geometries. For the minimum altitude case, this ratio ranged from 17 to 42, averaging ≈ 23 across the three geometries and sizes. For the maximum payload case, the typical value of this ratio was approximately 6, resulting in relative nozzle sizes shown in **Fig. 3**. Due to mass conservation, the outlet jet speed needs to be larger than the flow-through velocity by the same factor as precisely the A_{in}/A_{out} area ratio. Therefore, recalling the $v_{ft} \approx 0.03 I/P$ relationship, at the maximum payload altitude of 80 km, we can approximate $v_{jet} = v_{ft} A_{total}/A_{out} \approx 0.18 I/P \approx 0.18 \times 1300 W m^{-2}/1 Pa = 234 m/s$, while at the minimum altitude of 55 km (i.e., for zero payload), $v_{jet} = v_{ft} A_{total}/A_{out} \approx 0.70 I/P \approx 0.70 \times 1200 W m^{-2}/10 Pa = 84 m/s$. Notice that for the payload altitude of 80 km, the jet speed approaches but remains below the speed of sound, given by $v_{sound} = \sqrt{\gamma R_{air} T_{80km}} \approx \sqrt{1.4 \times 287 J/(kg K) \times 200 K} \approx 280 m/s$, where γ is the adiabatic constant of air, while $T_{80km} \approx 200 K$ is the air temperature at 80 km altitude. Achieving kg-scale payloads in the mesosphere will therefore require building 10m-scale photophoretic aircraft out of ultralight materials that simultaneously possess low areal densities ($\approx 1 g/m^2$) and sufficient structural integrity. However, these aircraft do not necessarily have to be rigid; instead, it is possible to make use of flexible parachute or balloon-like structures with overall dimensions similar to those shown in **Fig. 3**.

In the calculations above, we assumed that all surfaces are illuminated with $1000 W/m^2$ light intensity, which is not always realistic. The direct sunlight intensity in the mesosphere is similar to that in outer space, $\sim 1360 W/m^2$. Additional $\sim 500 W/m^2$ of sunlight will be reflected from the clouds and Earth below the aircraft due to Earth's planetary albedo of approximately 0.3. Depending on the elevation of the Sun in the sky and the orientation of the surface, it may be exposed to anywhere between essentially zero and almost $2000 W/m^2$ of combined direct and reflected sunlight. If the aircraft ends up rotating as balloons often do, all walls will experience an average flux on the order of $1000 W/m^2$ or slightly less. For reference, we also performed simulations at a reduced intensity of $500 W/m^2$, which results in payloads ~ 4 times lower than those shown above. One last important aspect to note about these photophoretic aircraft is that they only create lift when exposed to light (i.e., during the day), limiting the steady operation to ~ 12 hours at most latitudes, after which the aircraft will start to descend to the ground. However, near the poles, the polar day can last many months and extended operations of up to several months may be possible.

To conclude, we show that 3D photophoretic aircraft with porous walls made of ultralight, ultrathin materials are capable of carrying kg-scale payloads, comparable to those of typical CubeSats. The results presented above can be easily generalized for high-altitude operation on Mars using a Martian atmospheric model [22]. This work opens the way to creating persistent, low-cost, sensor-carrying aircraft in the previously inaccessible atmospheric regions at 55-80 km altitudes on Earth and 20-40 km altitudes on Mars, enabling a greater understanding of our planet and the worlds beyond.

References

- [1] Baum, S. D. (2009). Cost-benefit analysis of space exploration: Some ethical considerations. *Space Policy*, 25(2), 75-80. 8
- [2] Bainbridge, W. S. (2009). Motivations for space exploration. *Futures*, 41(8), 514-522.
- [3] Lindgren, E. A., Sheshadri, A., Podglajen, A., & Carver, R. W. (2020). Seasonal and latitudinal variability of the gravity wave spectrum in the lower stratosphere. *Journal of Geophysical Research: Atmospheres*, 125(18), e2020JD032850.
- [4] Laštovička, J. (2017). A review of recent progress in trends in the upper atmosphere. *Journal of Atmospheric and Solar-Terrestrial Physics*, 163, 2-13.

- [5] Bailey, S. M., Thuraiajah, B., Hervig, M. E., Siskind, D. E., Russell III, J. M., & Gordley, L. L. (2021). Trends in the polar summer mesosphere temperature and pressure altitude from satellite observations. *Journal of Atmospheric and Solar-Terrestrial Physics*, 220, 105650.
- [6] Tran, L. "NASA Satellites See Upper Atmosphere Cooling and Contracting." NASA. Goddard Space Flight Center, June 28, 2021. <https://www.nasa.gov/feature/goddard/2021/nasa-satellites-see-upper-atmosphere-cooling-contracting-climate-change>.
- [7] Goessling, H. F., & Bathiany, S. (2016). Why CO₂ cools the middle atmosphere—a consolidating model perspective. *Earth System Dynamics*, 7(3), 697-715.
- [8] Gohd, C. "Mars Helicopter Ingenuity: First Aircraft to Fly on Red Planet." Space.com. Space, May 22, 2021. <https://www.space.com/ingenuity-mars-helicopter-perseverance-rover>.
- [9] Squyres, S. W., Arvidson, R. E., Baumgartner, E. T., Bell III, J. F., Christensen, P. R., Gorevan, S., ... & Romero, R. A. (2003). Athena Mars rover science investigation. *Journal of Geophysical Research: Planets*, 108(E12).
- [10] Young, L. A., Delaune, J., Johnson, W., Withrow, S., Cummings, H., Sklyanskiy, E., ... & Bhagwat, R. (2020). Design Considerations for a Mars Highland Helicopter. In ASCEND 2020 (p. 4027).
- [11] Cortes, J., Stanczak, C., Azadi, M., Narula, M., Nicaise, S. M., Hu, H., & Bargatin, I. (2020). Photophoretic levitation of macroscopic nanocardboard plates. *Advanced Materials*, 32(16), 1906878.
- [12] Pharas, K., & McNamara, S. (2010). Knudsen pump driven by a thermoelectric material. *Journal of Micromechanics and Microengineering*, 20(12), 125032.
- [13] Lin, C., Nicaise, S. M., Lilley, D. E., Cortes, J., Jiao, P., Singh, J., ... & Bargatin, I. (2018). Nanocardboard as a nanoscale analog of hollow sandwich plates. *Nature communications*, 9(1), 1-8.
- [14] Horvath, H. (2014). Photophoresis—a forgotten force??? *KONA Powder and Particle Journal*, 31, 181-199.
- [15] European Space Agency. "Facts about Mars." https://www.esa.int/Science_Exploration/Space_Science/Mars_Express/Facts_about_Mars.
- [16] Niccolai, L., Bassetto, M., Quarta, A. A., & Mengali, G. (2019). A review of Smart Dust architecture, dynamics, and mission applications. *Progress in Aerospace Sciences*, 106, 1-14.
- [17] Azadi, M., Popov, G. A., Lu, Z., Eskenazi, A. G., Bang, A. J. W., Campbell, M. F., ... & Bargatin, I. (2021). Controlled levitation of nanostructured thin films for sun-powered near-space flight. *Science Advances*, 7(7), eabe1127.
- [18] Eskenazi, A., Celenza, T., & Bargatin, I. (2022). MATLAB-fluid-flow-parametric-studies. <https://github.com/andyeske/MATLAB-fluidflow-parametric-studies>
- [19] Engineering ToolBox. (2003). U.S. Standard Atmosphere vs. Altitude. https://www.engineeringtoolbox.com/standard-atmosphere-d_604.html
- [20] Saeed, N., Elzanaty, A., Almorad, H., Dahrouj, H., Al-Naffouri, T. Y., & Alouini, M. S. (2020). Cubesat communications: Recent advances and future challenges. *IEEE Communications Surveys & Tutorials*, 22(3), 1839-1862.
- [21] NASA. (2017). CubeSat 101: Basic Concepts and Processes for First-Time CubeSat Developers. https://www.nasa.gov/sites/default/files/atoms/files/nasa_csli_cubesat_101_508.pdf
- [22] Justh, H. L., Cianciolo, A. D., & Hoffman, J. (2021). Mars Global Reference Atmospheric Model (Mars-GRAM): User Guide (No. NASA/TM-20210023957).

3D photophoretic aircraft made from ultralight porous materials can carry kg-scale payloads in the mesosphere

Supplementary Information

Thomas Celenza, Andy Eskenazi and Igor Bargatin

In this document, we present and expand on the computational and theoretical framework behind our work. The first section is devoted to the ANSYS Fluent simulations, covering the solver set-up and the theory behind the force calculations. The second section of this document focuses on the MATLAB code, specifically the derivation of the equations used in the optimization of the geometrical and channel parameters of the 3D geometries, including the rocket, cone and sphere.

1. ANSYS Fluent Simulations

The goal of the ANSYS Fluent simulations was to determine an analytical expression to estimate the lift forces produced by various types of 3D structures. Because we sought geometries that operated across a wide range of velocities and altitudes (and thus air pressures, densities, temperatures and viscosities), the expression for the lift force needed to be valid across a wide range of Reynolds (Re) numbers as well. In particular, this equation needed to reasonably accurately model the transition between the low-Re (Stokes) regime to the high-Re regime. As the main paper argues, an appropriate expression is

$$F = C_1 8\mu D v_{ft} + C_2 \rho A v_{jet}^2. \quad (S1)$$

Here, μ corresponds to the fluid viscosity, ρ to the density, $A = \pi r^2$ is the area of a nozzle with radius r , D is the geometry's characteristic (usually largest) dimension, while v_{ft} is the flow-through velocity of the fluid through the porous material and v_{jet} is the velocity of the fluid exiting the structure through the small nozzle. The fitting parameters C_1 and C_2 depended on the geometry and were determined using ANSYS simulations. In this work, we considered three geometries, a cone, sphere, and rocket, shown in **Figure S1**.

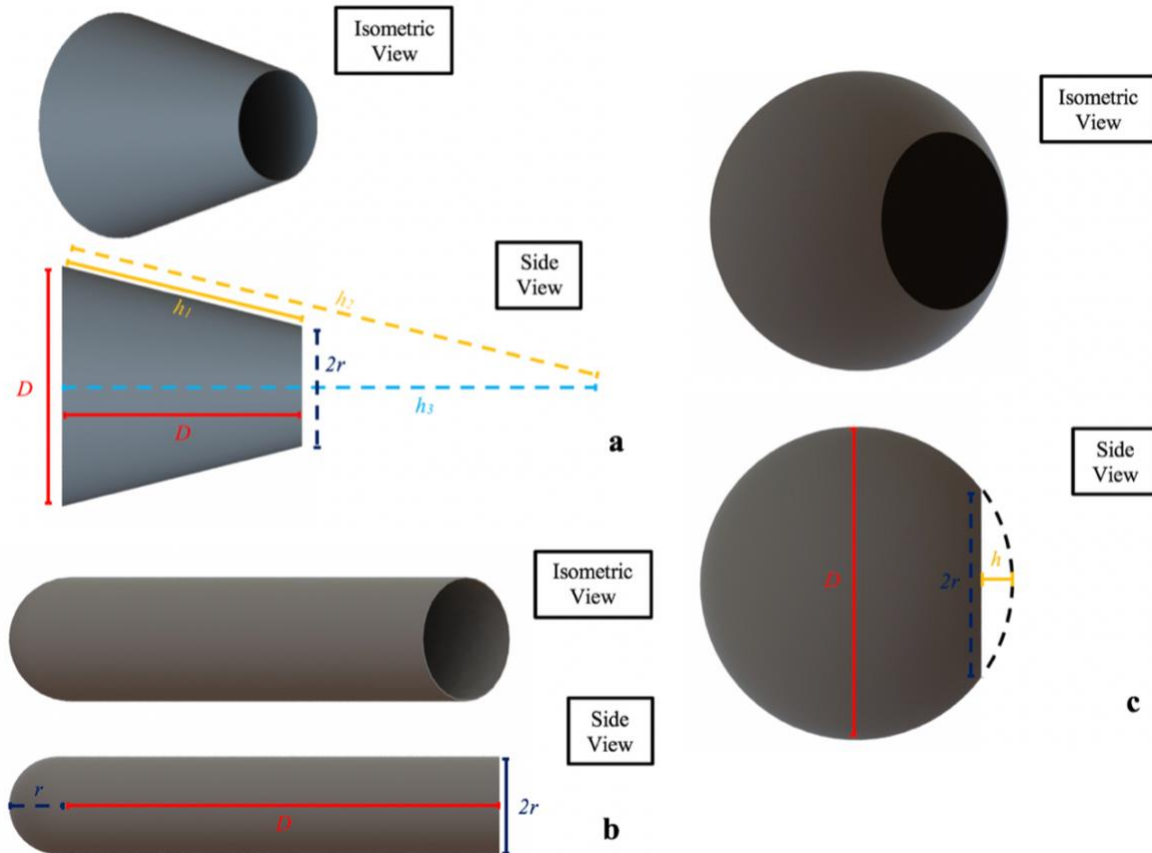


Figure S1: Main geometric parameters for the cone (a), rocket (b) and sphere (c). Notice that here, the variable D serves as an overall indicator of the size of the geometry, while the variable r controls the outlet radii of the nozzle.

Through the ANSYS Simulations, we determined the average C_1 and C_2 coefficients for each structure and examined how these would evolve with overall size of the structure or the altitude. We performed 9 sets of simulations for each geometry, where we varied three different inlet/outlet area ratios at three different altitudes, resulting in flow-through velocities as small as 10^{-6} m/s or as large as 1 m/s.

Figure S2 shows boundary conditions employed in our simulations using a sphere as an example. To make our simulations computationally more efficient, we took advantage of the axial symmetry of our three geometries and thus constructed our models in a 2D, axisymmetric environment, which allowed us to only simulate fluid flow on the top half of each structure. We formed these geometries using ANSYS' "Design Modeler" module, and they were essentially composed of three spaces: an outer air box, and inner air box, and the nanocardboard geometry itself (whose interior was "subtracted" from the inner air box, as seen in **Figure S2**).

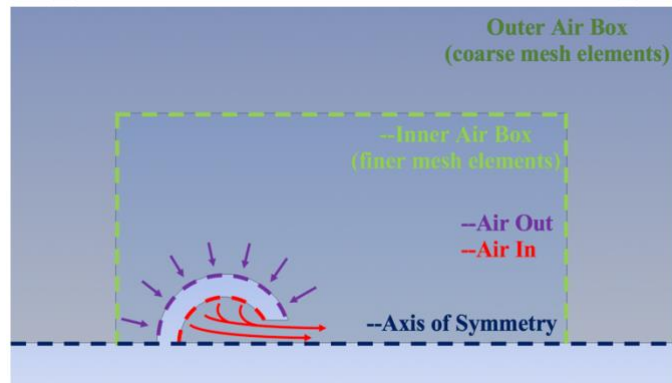


Figure S2: ANSYS Simulations boundary conditions. As the illustration shows, the inner wall of the geometry (red) was chosen as the flow-velocity inlet (inducing the air to flow from the into the structure), while the outer wall (violet) was selected as the outlet (mass outflow in Fluent, inducing the air to pass through the structure's walls). For the purposes of these simulations, we are assuming we have 100% porous walls through which the air flows at velocity v_{ft} (an idealization of the actual nanocardboard geometry).

The next step was to specify mesh elements, shown in **Figure S3**. Plot (a) shows the larger, outer air box with coarser mesh elements, while plot (b) is a zoomed-in view into the smaller, inner air box, containing smaller mesh elements. By dividing the air box into these two regions, we optimized the overall number of mesh elements in the simulation by providing a higher resolution just in the area close to the geometry. We created the mesh by selecting edges and dividing them into a discrete number of points; to enforce a uniform grid pattern, we used the quadrilaterals face meshing command. For the sphere, this resulted in 184,180 elements (185,408 nodes); for the cone, 194,322 elements (195,865 nodes); for the rocket, 293,053 elements (294,616 nodes). These were the final numbers of mesh elements obtained as a result of performing a convergence analysis until observing negligible changes in the computed lift forces.

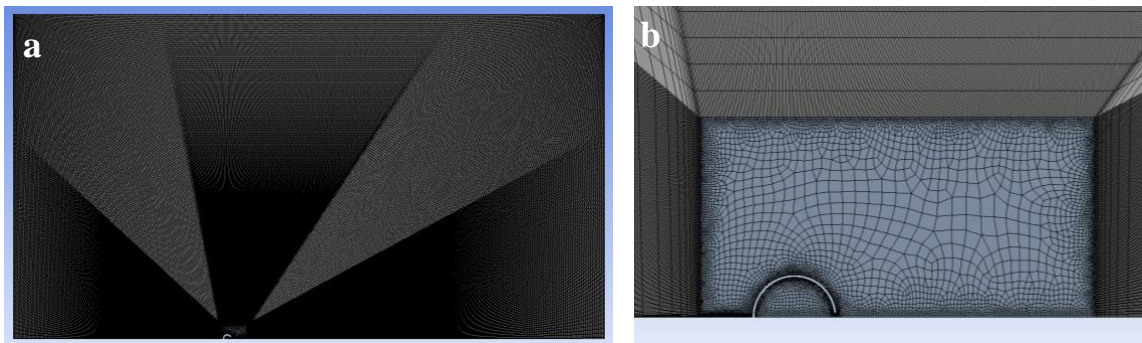


Figure S3: Sample meshing of the axisymmetric sphere simulation in ANSYS Fluent. Here, plot (a) provides an overall picture of the air box (which is more than ten times larger than the geometry in question in each dimension), while plot (b) shows a zoomed-in image of the area immediately surrounding the sphere. The size of the outer air box was not arbitrary, but rather resulted from a series of simulations that gradually increased its dimensions until force values converged.

The final step was to establish Fluent's "set-up" module parameters. For the model, we chose the viscous k-omega, with the low-Re (viscous) corrections feature enabled. Next, we fixed the boundary conditions as described by **Figure S2**, and manually modified operating conditions (environment pressure, fluid density and fluid viscosity) matching the chosen altitude. Since our fluid was air, we extracted its properties as tabulated in altitude-dependent standard atmospheric tables, summarized in **Table 1** below for 0 km, 40 km and 70 km (our probed altitudes). Last, we specified the inlet velocity as a variable parameter, since that

allowed us to sweep through values ranging from 10^{-6} m/s to 1 m/s in 7 logarithmically equally spaced points.

Summary of Altitude-Dependent Atmospheric Properties			
Altitude	0 km	40 km	70 km
Atmospheric Pressure (Pa)	101300	275.47	4.66
Atmospheric Temperature (K)	288	251	220
Air Density (kg/m ³)	1.23	$3.83 \cdot 10^{-3}$	$7.38 \cdot 10^{-5}$
Air Viscosity (Pa * s)	$1.796 \cdot 10^{-5}$	$1.610 \cdot 10^{-5}$	$1.447 \cdot 10^{-5}$

Table 1: Tabulated altitude-dependent atmospheric conditions for 0 km, 40 km and 70 km. These values were manually inputted for each simulation set into the Fluent solver.

We repeated this process 36 times, to construct 18 simulations for the cone, 9 for the sphere and 9 for the rocket, using operating conditions corresponding to 3 different altitudes (0 km, 40 km and 70 km) and 3 different geometry sizes. In each case, we computed the reaction force in the axisymmetric direction using a line integral along the walls of the outer air box, resulting in the force values shown in **Figures S4–S7**. This computation made use of the fact that under steady-state operation, the reaction force is equal to the lift force. The C_1 and C_2 coefficients were then determined by performing a non-linear fitting in MATLAB to equation (S1), resulting in the values that are shown in the same figures and tabulated in **Tables 2-5**. In general, most curves of **Figures S4–S7** (in the logarithmic scale) show a transition from the viscous, low-Re regime to the high-Re regime that is manifested through a change in the slopes of the force curves. However, at 70 km in altitude, the lift force stayed in the Stokes (low-Re) regime and the high-Re C_2 coefficients remained uncertain at this particular altitude. Thus, when computing the overall average C_1 and C_2 , we did not incorporate the C_2 corresponding to the 70 km altitude.

Fitting Parameters for the Rocket, Dia. = 2 cm						
Altitude	Length = 1 cm		Length = 5 cm		Length = 10 cm	
	C_1	C_2	C_1	C_2	C_1	C_2
0 km	2.0 (1.6–2.4)	1.1 (0.9–1.3)	1.0 (0.8–1.2)	1.1 (0.9–1.2)	0.9 (0.7–1.1)	1.1 (0.9–1.2)
40 km	2.24 (2.12–2.38)	0.73 (0.62–0.85)	1.1 (1.0–1.3)	0.8 (0.6–1.0)	1.0 (0.9–1.2)	0.8 (0.6–1.0)
70 km	2.361 (2.353–2.368)		1.20 (1.20–1.20)		1.08 (1.08–1.10)	
Average	2.22	0.91	1.12	0.92	1.00	0.95

Table 2: C_1 and C_2 coefficients computed for the rocket geometry of different lengths (1 cm, 5 cm and 10 cm), alongside the 66% confidence intervals for each fitting parameter (tabulated below each coefficient entry).

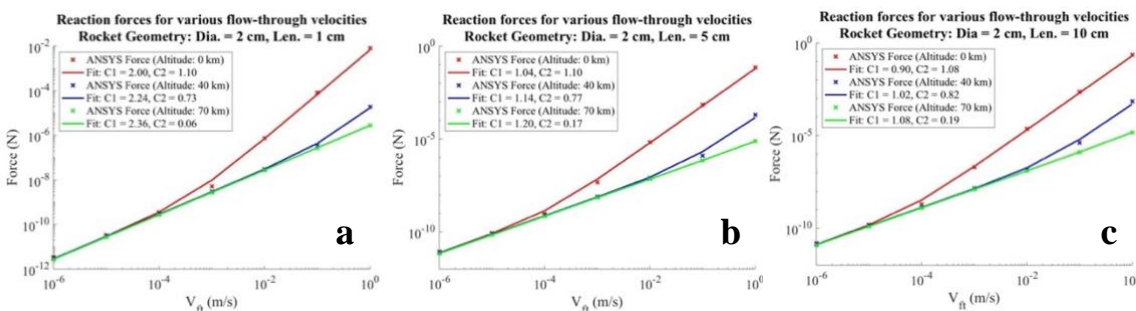


Figure S4: Results from the altitude-dependent rocket simulations in ANSYS Fluent; each data point corresponds to a different flow-through velocity, ranging from 10^{-6} m/s to 1 m/s, while plots (a), (b) and (c) correspond to different rocket lengths.

Fitting Parameters for the Sphere, Dia. = 2 cm						
Altitude	$r_{out} = 0.1$ cm		$r_{out} = 0.5$ cm		$r_{out} = 1$ cm	
	C_1	C_2	C_1	C_2	C_1	C_2
0 km	1.4 (0.7–2.0)	0.29 (0.21–0.37)	1.5 (1.3–1.7)	1.06 (0.95–1.18)	0.9 (0.8–1.0)	1.5 (1.4–1.7)
40 km	1.4 (1.0–1.9)	0.6 (0.4–0.8)	1.5 (1.3–1.6)	0.9 (0.7–1.0)	0.91 (0.89–0.93)	0.99 (0.91–1.08)
70 km	1.65 (1.63–1.67)		1.58 (1.52–1.64)		0.95 (0.94–0.96)	
Average	1.48	0.45	1.50	0.97	0.91	1.26

Table 3: C_1 and C_2 coefficients computed for the sphere geometry of different outlet radii (0.1 cm, 0.5 cm and 1 cm), alongside the 66% confidence intervals for each fitting parameter (tabulated below each coefficient entry).

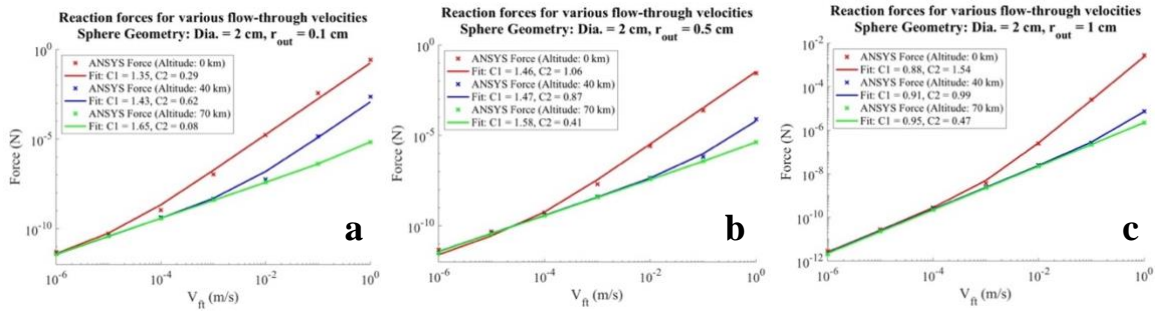


Figure S5: Results from the altitude-dependent sphere simulations in ANSYS Fluent; each data point corresponds to a different flow-through velocity, ranging from 10^{-6} m/s to 1 m/s, while plots (a), (b) and (c) correspond to different sphere outlet radii.

Fitting Parameters for the Cone, Dia. = 2 cm						
Altitude	Length = 2 cm		Length = 5 cm		Length = 10 cm	
	C_1	C_2	C_1	C_2	C_1	C_2
0 km	0.7 (0.5–1.0)	0.9 (0.7–1.1)	0.7 (0.5–0.9)	0.9 (0.8–1.1)	0.7 (0.4–1.0)	0.9 (0.7–1.1)
40 km	1.0 (0.8–1.2)	0.6 (0.3–0.8)	0.9 (0.7–1.1)	0.6 (0.4–0.8)	0.8 (0.7–1.0)	0.7 (0.6–0.9)
70 km	1.07 (0.98–1.16)		1.01 (0.94–1.07)		0.98 (0.95–1.02)	
Average	0.94	0.72	0.88	0.76	0.84	0.82

Table 4: C_1 and C_2 coefficients computed for the cone geometry (2 cm diameter) of different lengths (2 cm, 5 cm and 10 cm), alongside the 66% confidence intervals for each fitting parameter (tabulated below each coefficient entry).

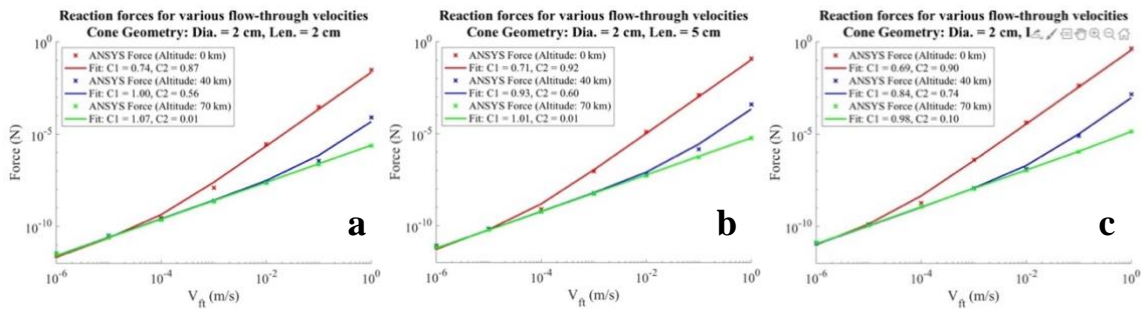


Figure S6: Results from the altitude-dependent cone (2 cm diameter) simulations in ANSYS Fluent; each data point corresponds to a different flow-through velocity, ranging from 10^{-6} m/s to 1 m/s, while plots (a), (b) and (c) correspond to different cone lengths.

Fitting Parameters for the Cone, Dia. = 4 cm						
Altitude	Length = 2 cm		Length = 5 cm		Length = 10 cm	
	C_1	C_2	C_1	C_2	C_1	C_2
0 km	0.9 (0.7–1.1)	1.0 (0.8–1.2)	1.0 (0.8–1.2)	1.0 (0.8–1.1)	1.0 (0.7–1.3)	1.0 (0.8–1.1)
40 km	1.4 (1.1–1.7)	0.6 (0.4–0.9)	1.2 (1.0–1.3)	0.7 (0.6–0.9)	1.1 (1.0–1.2)	0.8 (0.7–1.0)
70 km	1.5 (1.3–1.6)		1.24 (1.22–1.25)		1.19 (1.18–1.20)	
Average	1.27	0.82	1.13	0.86	1.09	0.89

Table 5: C_1 and C_2 coefficients computed for the cone geometry (4 cm diameter) of different lengths (2 cm, 5 cm and 10 cm), alongside the 66% confidence intervals for each fitting parameter (tabulated below each coefficient entry).

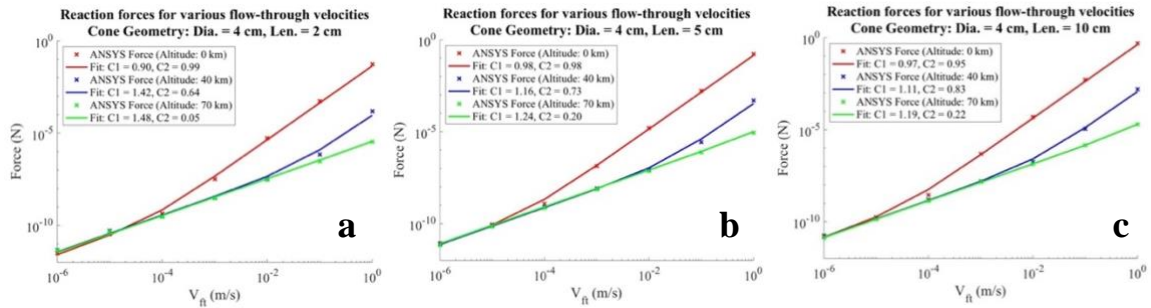


Figure S7: Results from the altitude-dependent cone (4 cm diameter) simulations in ANSYS Fluent; each data point corresponds to a different flow-through velocity, ranging from 10^{-6} m/s to 1 m/s, while plots (a), (b) and (c) correspond to different cone lengths.

As we increased in altitude, the value of the C_1 parameter increased while that of C_2 decreased. All in all, **Table 6** below summarizes the average C_1 and C_2 coefficients obtained for each geometry. In all cases, the coefficients are on the order of 1.

Average Fitting Parameters for Each Geometry				
Geometry	Cone		Sphere	Rocket
	$D = 2$ cm	$D = 4$ cm	$D = 2$ cm	$D = 2$ cm
C_1	0.9	1.2	1.3	1.4
C_2	0.8	0.9	0.9	0.9

Table 6: Fitting parameters for the analytical theory for standard atmospheric conditions on Earth, for each geometry.

To verify our simulations were based on realistic boundary conditions, we examined the streamline plots generated in ANSYS Fluent’s results module, a sample of which is shown in **Figure S8** below.

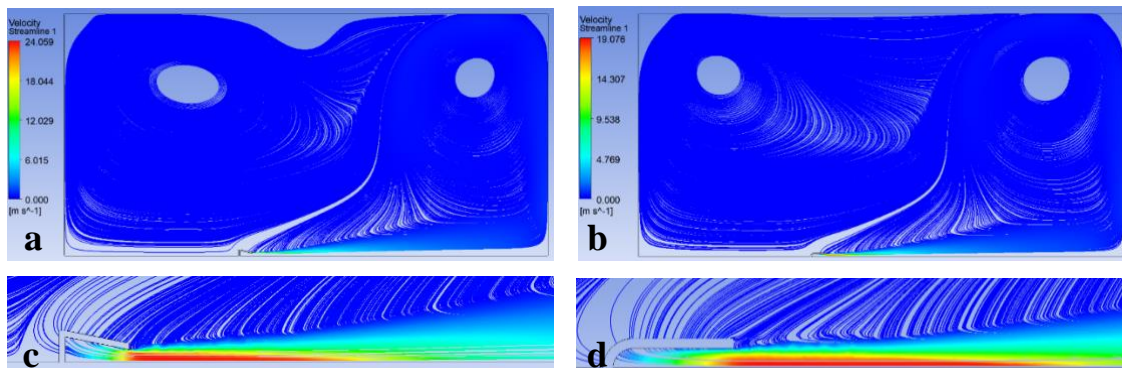


Figure S8: Velocity streamlines corresponding to the cone (a, c) and rocket (b, d) geometries simulations in ANSYS, for a flow-through velocity of 1 m/s and atmospheric conditions corresponding to 0 km in altitude. Both the cone and rocket have a characteristic dimension (D) of 5 cm. (c) and (d) denote a zoomed-in view of plots (a) and (b), respectively.

As expected, a jet of high-speed air exited the geometries as a result of the air flowing in through the porous structures. Once the air left the geometry, it interacted with the walls of the outer air box by forming large vortices, as anticipated for a fluid circulating in a contained box.

The next section of this document takes the force fitting parameters found from the ANSYS Fluent simulations and focuses on MATLAB-based parametric optimization of our three different geometries.

2. MATLAB Code and Extension of Theoretical Framework

In this section of the supplementary information, we present the extension to 3D structures of the original nanocardboard fluid mechanic theory developed by [R3]. The equations derived below were implemented in a MATLAB code to perform a series of parametric studies that seek to optimize the geometric and porous parameters of our three study geometries, a cone, a sphere and a rocket. More information about our code can be found in our [publicly available repository](#) [R4].

2.1. Derivation of Equations

2.1.1 General Overview

For a general 3D porous structure, conservation of mass establishes that

$$A_{total}v_{ft} = A_{out}v_{out} . \quad (S2)$$

Here, A_{total} represents the total surface area of the structure (as if the structure had no pores/channels) and v_{ft} is the flow-through velocity of the fluid across this surface. Similarly, A_{out} corresponds to the area covered by the outlet, while v_{out} is the exit velocity of the fluid out of the structure. Adding Bernoulli's equation, we get the relationship that

$$\frac{P_{in} - P_{out}}{\rho} = \frac{\Delta P}{\rho} = \frac{v_{out}^2 - v_{ft}^2}{2} . \quad (S3)$$

In (S5), P_{in} is the pressure right at the inlet of the structure, P_{out} is the pressure right as the jet of fluid is leaving the structure, located around the space close to A_{out} , while ρ is the fluid density. This equation can be rearranged to yield an expression for the pressure difference across both ends of the structure, resulting in

$$\Delta P = \frac{\rho(v_{out}^2 - v_{ft}^2)}{2} . \quad (S4)$$

Assuming that the porosity of the 3D structure originates from using the nanocardboard geometry developed by [R3] as the wall material, then we can model the mass flow rate of the fluid across one of the structure's pores (or more properly said, channels) using the following equation

$$\dot{m} = -\alpha * \Delta P + \gamma * \Delta T . \quad (S5)$$

In (S5), α and γ represent two constants, which take the following forms¹:

$$\alpha = \left(\frac{\delta}{6} + 1\right) \left(1 + \frac{0.25}{\sqrt{\delta}}\right) \frac{A^2 B \beta_*}{L} , \quad (S6)$$

and

$$\gamma = \left(\frac{1.1}{1.5 + \delta}\right) \frac{A^2 B P_* \beta_*}{T_* L} . \quad (S7)$$

¹ The variables α and γ come from curve-fitting the data from by [R7] and transforming the non-dimensional flow rate equation into a dimensional form again, with both pressure and temperature contributions. For more information, please see [R2].

Here, the variable P_* denotes the average pressure² between the two sides of the structure's nanocardboard wall, T_* analogously describes the average temperature between both sides of the wall's surface, while β_* is an inverse velocity parameter. Specifically, this last one is given by

$$\beta_* = \sqrt{\frac{m}{2k_B T_*}}, \quad (\text{S8})$$

where k_B is the Boltzmann constant (equal to $1.38 * 10^{-23}$ J/K), and m is the mass of an air molecule³. Lastly, the parameter δ is the gas rarefaction coefficient, which [R7] defines as

$$\delta = \frac{\sqrt{\pi} A}{2\lambda} = \frac{\sqrt{\pi}}{2Kn}. \quad (\text{S9})$$

In this expression, λ is the molecular mean free path, defined as the average distance traveled by a molecule between collisions with other molecules, and Kn is the Knudsen number, which is characterized in terms of the channel width. In essence, higher values of the δ parameter designates flows in the continuum regime, while smaller values indicate flows taking place in the free molecular regime. As for the molecular mean free path, mathematically it is usually expressed as

$$\lambda = \frac{\mu(T)}{P(T)} \sqrt{\frac{\pi k_B T}{2m}} = \frac{\mu(T)}{P(T)} \sqrt{\frac{\pi R_{air} T}{2}}, \quad (\text{S10})$$

where $\mu(T)$ is the fluid's viscosity and $P(T)$ is the operating pressure, both given as a function of T , the operating temperature. In addition, from equation (S9), we see the Knudsen number is defined as

$$Kn = \frac{\lambda}{A}. \quad (\text{S11})$$

Additionally, as seen in **Figure S9** below, the variables A and B characterize the nanocardboard channel's width and length, respectively, yielding a cross-sectional area of $A \times B$. In addition, L denotes the channel's height. Note that in [R3], A is assumed to be much smaller than B .

After defining these variables and introducing the expression for the mass flow rate, \dot{m} , across one of nanocardboard's channels, then an equation can be derived for the average flow-through velocity across the structure's surface, which is simply described by

$$v_{ft} = \frac{\varphi \dot{m}}{\rho AB} = \frac{\varphi(-\alpha \Delta P + \gamma \Delta T)}{\rho AB}. \quad (\text{S12})$$

Here, \dot{m}/ρ is no other than the volumetric flow rate \dot{V} , while the term φ denotes the geometric fill factor, which is defined in terms of A_{in} (porous area) and A_{total} ⁴, or the channel parameters, and takes the form

$$\varphi = \frac{A_{in}}{A_{total}} = \frac{ABX}{(ABX + SBX)} = \frac{A}{(A + S)}. \quad (\text{S13})$$

The latter two equivalencies in (S13) originates from analyzing a single nanocardboard unit cell as opposed to the full 3D structure. Indeed, as **Figure S9** shows, the total cross-sectional area of the cell (if no channels were present) is given by

$$A_{cell} = (ABX + SBX) = (A + S)BX, \quad (\text{S14})$$

where the variable X is just the number of channels in a unit cell.

² The value of this variable may be found from performing CFD simulations but will be simply approximated as the operating pressure.

³ The molar mass of air is 0.02896 kg/mol, so then the approximated mass of an air molecule would be $0.02896/(6.022 * 10^{23})$ (Avogadro's number), or $4.8089 * 10^{-26}$ kg.

⁴ This area is essentially the total 3D structure wall area if there were no channels present. This is analogous to A_{cell} in the single nanocardboard unit cell.

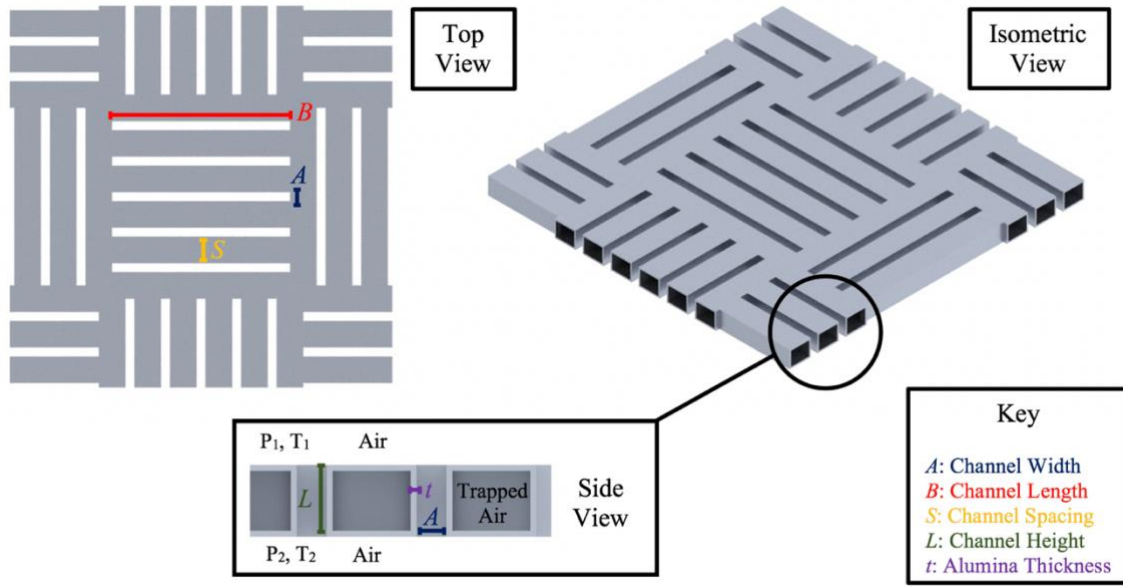


Figure S9: Main nanocardboard channel parameters.

However, this number (X) is not arbitrarily chosen, and is dictated by A , B and S in the following way

$$X = \frac{B - S}{S + A}. \quad (S15)$$

This expression considers the channel width A and spacing S as a unit, and tries to fit as many of those $A + S$ units into the channel length B . Nonetheless, we need to consider an additional S for spacing against the perpendicular channels. This can be seen more clearly in **Figure S10** below, where the yellow bars represent the $A + S$ units, and as drawn, five of these fit in the length of B , after subtracting one S .

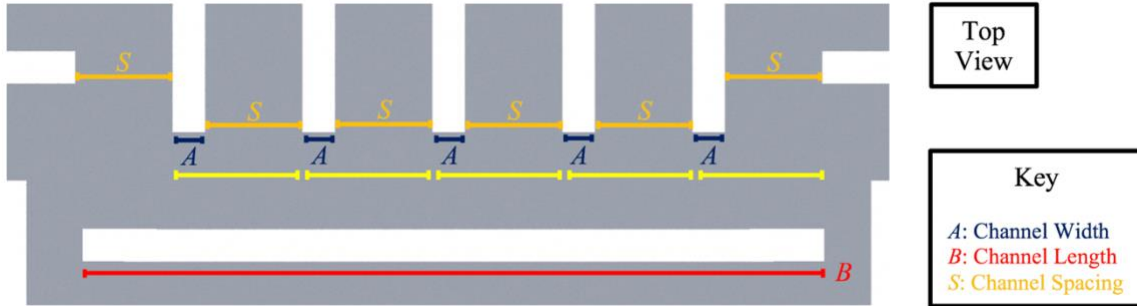


Figure S10: Illustration of equation (S15), with the yellow bars showing the $A + S$ units fitted into the channel length B .

Overall, the flow-through velocity expression provided in (S12) is a step closer towards calculating the lift force that a 3D structure could generate for a given combination of geometric and channel parameters. However, computing lift will not be possible until we solve for v_{out} . Therefore, (S12) can be rearranged to instead solve for another unknown, ΔP , and obtain

$$\Delta P = \frac{\gamma \Delta T}{\alpha} - \frac{v_{ft} \rho A B}{\alpha \varphi}. \quad (S16)$$

Since both (S16) and (S4) from above provide two distinct expressions for the pressure difference, it is possible to equate them, giving rise to yet another relationship between v_{ft} and v_{out} , giving

$$\frac{\rho(v_{out}^2 - v_{ft}^2)}{2} = \Delta P = \frac{\gamma\Delta T}{\alpha} - \frac{v_{ft}\rho AB}{\alpha\varphi}. \quad (S17)$$

Rearranging this expression further, we get

$$v_{out}^2 = \frac{2}{\rho} \left(\frac{\gamma\Delta T}{\alpha} - \frac{v_{ft}\rho AB}{\alpha\varphi} \right) + v_{ft}^2. \quad (S18)$$

Now, recalling the conservation of mass relationship provided in (S2), it is possible to write v_{ft} , the flow-through velocity across the channels, in terms of v_{out}

$$v_{ft} = \frac{A_{out}}{A_{total}} v_{out} = \frac{\varphi A_{out}}{A_{in}} v_{out}. \quad (S19)$$

Thus, (S19) can replace the v_{ft} term in (S18), leaving everything in terms of just v_{out}

$$v_{out}^2 = \frac{2}{\rho} \left(\frac{\gamma\Delta T}{\alpha} - \frac{A_{out}v_{out}\rho AB}{A_{total}\alpha\varphi} \right) + \left(\frac{A_{out}}{A_{total}} \right)^2 v_{out}^2. \quad (S20)$$

Further manipulating (S20), we get the following quadratic

$$v_{out}^2 \left(1 - \left(\frac{A_{out}}{A_{total}} \right)^2 \right) + v_{out} \left(\frac{2A_{out}AB}{A_{total}\alpha\varphi} \right) - \frac{2\gamma\Delta T}{\rho\alpha} = 0, \quad (S21)$$

which has precisely v_{out} as its only unknown. The coefficients of this polynomial are

$$a = 1 - \left(\frac{A_{out}}{A_{total}} \right)^2, \quad b = \frac{2A_{out}AB}{A_{total}\alpha\varphi}, \quad c = -\frac{2\gamma\Delta T}{\rho\alpha}, \quad (S22)$$

making it a fairly straightforward process to solve for the roots of the equation, provided by

$$v_{out} = \frac{-\left(\frac{2A_{out}AB}{A_{total}\alpha\varphi} \right) \pm \sqrt{\left(\frac{2A_{out}AB}{A_{total}\alpha\varphi} \right)^2 + \frac{8\gamma\Delta T}{\rho\alpha} \left(1 - \left(\frac{A_{out}}{A_{total}} \right)^2 \right)}}{2 \left(1 - \left(\frac{A_{out}}{A_{total}} \right)^2 \right)}. \quad (S23)$$

One underlying advantage of this derivation was that it removed the need to know the pressure difference, ΔP , while providing us with enough information to solve for v_{out} and v_{ft} . In the following sub-section, we deliver more details on the heat conduction modeling across the nanocardboard's thickness, which enabled obtaining an expression for the temperature difference, ΔT , necessary to solve for v_{out} in (S23).

2.1.2 Heat Conduction Modeling

2.1.2.1 Full Analytical Derivation for ΔT

In order to compute ΔT , the temperature difference between both sides of the structure's walls, we needed to model the heat conduction across the structure's thickness. We performed a heat energy balance that considered heat transfer across three distinct cross-sectional areas: the channel's column of air, across the alumina thickness of the channel, and across the air trapped within the structure, as shown in **Figure S11** below. As a result, we can let Q_t , the total heat transfer, be

$$Q_t = \frac{\Delta T}{R_{t1}} + \frac{\Delta T}{R_{t2}} + \frac{\Delta T}{R_{t3}}, \quad (S24)$$

where the R_{t1} , R_{t2} and R_{t3} represent the thermal resistances under the three scenarios detailed above.

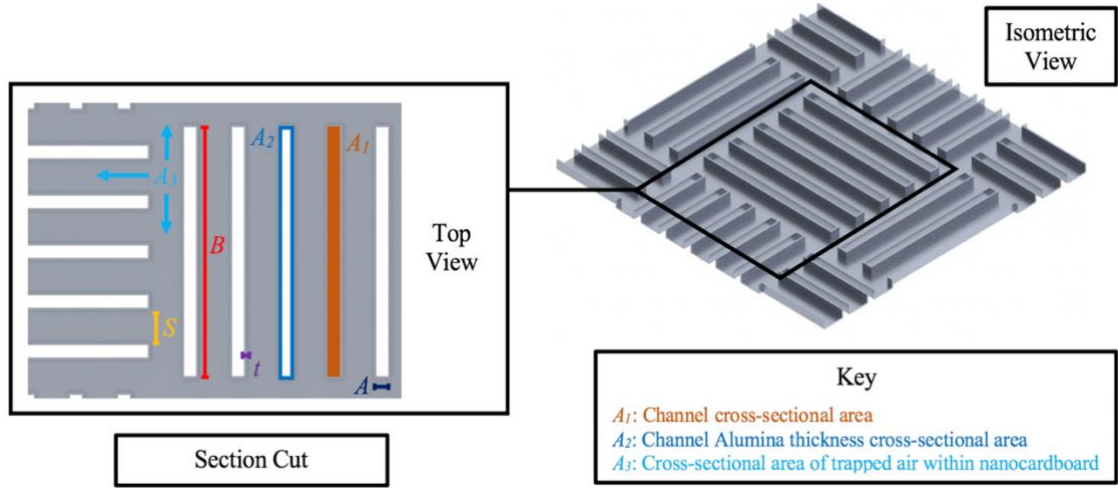


Figure S11: Main nanocardboard cross-sectional areas for which thermal resistance is calculated.

For the first of these areas (A_1), the column of air in the channel, we define its thermal resistance as

$$R_{t1} = \frac{L}{k_{air}A_1X} = \frac{L}{k_{air}ABX}, \quad (S25)$$

where k_{air} is the thermal conductivity of air, L is as usual the channel height, and ABX is the cross-sectional area of the individual channels multiplied by the number of channels in a unit cell, as shown in **Figure S9** above. Notice that k_{air} is both temperature and pressure dependent, as the equation developed by [R10] captures, specifically for the small MEMS scale:

$$k_{air} = \frac{\kappa_0}{\left(1 + \frac{0.00076T}{PL}\right)}. \quad (S26)$$

In this expression, κ_0 is the air conductivity at standard atmospheric conditions, normally quoted as $\kappa_0 = 0.024 \frac{W}{mK}$. Another comparable and slightly more succinct model for the conductivity of air is from [R8]:

$$k_{air} = \frac{\kappa_0}{\left(1 + \frac{3.116\lambda}{L}\right)}. \quad (S27)$$

As the pressure decrease, the mean free path eventually becomes comparable to the channel length, and the effective conductivity starts to decrease below the continuum value. Both equations (S26) and (S27) yielded very similar values for the conductivity of air as a function of the channel thickness L , although we used Eq. S27 in the simulations.

Continuing with the heat conduction modeling, the corresponding expression for the thermal resistance across the alumina thickness on the channels (area A_2 in **Figure S11**) is given by

$$R_{t2} = \frac{L}{k_{ald}A_2X} = \frac{L}{k_{ald}[(A + 2t)(B + 2t) - AB]X}, \quad (S28)$$

where $[(A + 2t)(B + 2t) - AB]X$ is the cross-sectional area occupied by the alumina thickness of the channels, which is denoted as t . In (S28), k_{ald} is the thermal conductivity of alumina, which has a constant value of $1.8 \frac{W}{mK}$ [R2]. Lastly, the thermal resistance of the air trapped within the structure (area A_3) is

$$R_{t3} = \frac{L - 2t}{k_{air}A_3} = \frac{L - 2t}{k_{air} \left[\frac{AB}{\phi} - (A + 2t)(B + 2t) \right] X}, \quad (S29)$$

where recall from (S13) that $\frac{ABX}{\varphi}$ is the full area of the cell, from which we subtract the combined cross-sectional area of the channels with thickness t of alumina. Now, performing an energy balance, the heat flow through the structure's walls must be equal to that from the absorbed irradiation of the sun, which in this case is given by

$$Q_t = \varepsilon\psi I_{sun} \left(\frac{ABX}{\varphi} \right) (1 - \varphi). \quad (S30)$$

In equation (S30), ε denotes the absorption coefficient (approximated to 0.9 based-off the measurements from [R3]), ψ the proportion of absorbed optical flux dissipated upward through the nanocardboard (which is assumed to be 0.5 or 50%), and I_{sun} the intensity of the sun at a particular altitude. In particular, this last term can be modeled using the following equation

$$I_{sun} = 1000 + 3.8h, \quad (S31)$$

where the variable h refers to the elevation above sea level in kilometers. Notice that this expression returns the sun's intensity in units of Watts per meter square. Furthermore, in equation (S30), $(ABX/\varphi)(1 - \varphi)$ corresponds to the solid area of the nanocardboard, A_{solid} , where the sun's irradiation is absorbed. In any case, (S24) through (S31) were combined to write a general expression for ΔT , which is summarized by

$$\begin{aligned} \Delta T = T_2 - T_1 &= \frac{\varepsilon\psi I_{sun} \left(\frac{ABX}{\varphi} \right) (1 - \varphi)}{\frac{1}{R_{t1}} + \frac{1}{R_{t2}} + \frac{1}{R_{t3}}} = \\ &= \frac{\varepsilon\psi I_{sun} \left(\frac{ABX}{\varphi} \right) (1 - \varphi)}{\frac{k_{air}ABX}{L} + \frac{k_{ald}[(A + 2t)(B + 2t) - AB]X}{L} + \frac{k_{air} \left[\frac{AB}{\varphi} - (A + 2t)(B + 2t) \right] X}{L - 2t}}. \end{aligned} \quad (S32)$$

In (S32), T_1 and T_2 represent the average temperatures outside and inside the 3D structure, respectively. However, these might not necessarily be known beforehand, reason why calculating ΔT or T_* , the average temperature between both sides of the surface, may not be as trivial. In particular, to compute T_* , we make use of the fact that we know what ΔT is from (S32) and take the following expression

$$T_* = \frac{T_1 + T_2}{2} = \frac{(T_2 - T_1) + 2 * T_1}{2} = \frac{\Delta T + 2 * T_1}{2}. \quad (S33)$$

Here, notice that T_1 is simply equal to the temperature corresponding to the particular operating conditions (altitude, pressure, density) of the fluid. Overall, ΔT allows us to solve for T_* (which is needed to compute γ and β_* in (S7) and (S9), respectively) and the last part of the puzzle in (S23), the v_{out} expression.

2.1.2.2 Simplified Expression for ΔT in the limit of zero alumina thickness

Beyond the derivation provided in 1.2.1, notice that one could potentially also approximate ΔT through a more simplified expression given by

$$\Delta T \sim \frac{LI_{sun}(1 - \varphi)}{2\kappa_{air}}. \quad (S34)$$

The origin of (S34) comes from taking the limit as t , the alumina thickness, approaches zero, in equation (S32). Indeed,

$$\lim_{t \rightarrow 0} \frac{\varepsilon\psi I_{sun} \left(\frac{ABX}{\varphi} \right) (1 - \varphi)}{\frac{k_{air}ABX}{L} + \frac{k_{ald}[(A + 2t)(B + 2t) - AB]X}{L} + \frac{k_{air} \left[\frac{AB}{\varphi} - (A + 2t)(B + 2t) \right] X}{L - 2t}} \quad (S35)$$

$$\begin{aligned}
&= \lim_{t \rightarrow 0} \frac{L\varepsilon\psi I_{sun} \left(\frac{ABX}{\varphi} \right) (1 - \varphi)}{k_{air} ABX + k_{ald} [(A + 2t)(B + 2t) - AB]X + k_{air} \left[\frac{AB}{\varphi} - (A + 2t)(B + 2t) \right] X} \\
&= \lim_{t \rightarrow 0} \frac{L\varepsilon\psi I_{sun} \left(\frac{ABX}{\varphi} \right) (1 - \varphi)}{k_{air} ABX + k_{ald} [AB - AB]X + k_{air} \left[\frac{AB}{\varphi} - AB \right] X} \\
&= \lim_{t \rightarrow 0} \frac{L\varepsilon\psi I_{sun} \left(\frac{ABX}{\varphi} \right) (1 - \varphi)}{k_{air} ABX + k_{air} \frac{ABX}{\varphi} - k_{air} ABX} = \frac{L\varepsilon\psi I_{sun} \left(\frac{ABX}{\varphi} \right) (1 - \varphi)}{k_{air} \frac{ABX}{\varphi}} \\
&= \frac{L\varepsilon\psi I_{sun} (1 - \varphi)}{k_{air}}.
\end{aligned}$$

Furthermore, letting $\varepsilon = 1$ and $\psi = 0.5$, then (S37) indeed becomes equation (S34) from above. As evidenced by its compressed form, using (S36) to approximate ΔT simplifies the process of solving for the flow-through velocity, v_{ft} . This is especially true if we were to also neglect the pressure term, assuming its contribution is negligible. As a result, the mass flow rate from (S5) can be re-written as

$$\dot{m} \sim \gamma * \Delta T. \quad (S36)$$

This helps reduce the flow-through velocity expression to

$$v_{ft} = \frac{\varphi \dot{m}}{\rho AB} = \frac{\varphi \gamma \Delta T}{\rho AB} = \frac{\varphi \gamma LI_{sun} (1 - \varphi)}{\rho AB 2\kappa_{air}}. \quad (S37)$$

Even this expression can be further simplified by reducing the γ term from (S7) to

$$\gamma \sim \frac{1.1A^2 BP_* \beta_*}{\delta T_* L} = \frac{1.1A^2 BP_* \beta_*}{TLA\sqrt{\pi}/(2\lambda)} = \frac{2.2\lambda ABP}{\sqrt{\pi} TL} \sqrt{\frac{m}{2k_B T}}. \quad (S38)$$

From the ideal gas law, we have that $P = \rho R_{air} T$, so the pressure term can be replaced in (S38) to obtain

$$\gamma \sim \frac{2.2\lambda AB \rho R_{air} T}{\sqrt{\pi} TL} \sqrt{\frac{m}{2k_B T}} = \frac{2.2\lambda AB \rho R_{air}}{\sqrt{\pi} L} \sqrt{\frac{m}{2k_B T}}. \quad (S39)$$

Combining equations (S37) and (S39), we resultant expression turns out as

$$v_{ft} = \frac{\varphi}{\rho AB} \frac{LI(1 - \varphi)}{2\kappa_{air}} \frac{2.2\lambda AB \rho R_{air}}{\sqrt{\pi} L} \sqrt{\frac{m}{2k_B T}} = \frac{1.1\varphi I(1 - \varphi) \lambda R_{air}}{\kappa_{air}} \sqrt{\frac{m}{2k_B T \pi}} \quad (S40)$$

Now, recall that the average molecular velocity is equal to

$$v_{avg} = \sqrt{\frac{8R_{air} T}{\pi}}, \quad (S41)$$

and the relationship between viscosity and velocity, as provided by [R6], is equal to

$$\mu = \frac{\lambda \rho v_{avg}}{2}. \quad (S42)$$

Hence, combining both (S41) and (S42) and solving for λ , we obtain an expression which can be incorporated in (S40) to yield

$$\begin{aligned} v_{ft} &= \frac{1.1\varphi I(1-\varphi)R_{air}\mu}{\kappa_{air}} \frac{1}{P} \sqrt{\frac{\pi k_B T}{2m}} \sqrt{\frac{m}{2k_B T \pi}} = \frac{1.1\varphi I(1-\varphi)R_{air}\mu}{\kappa_{air}} \frac{1}{P} \sqrt{\frac{m\pi k_B T}{4k_B T \pi m}} \\ &= \frac{1.1\varphi I(1-\varphi)R_{air}\mu}{\kappa_{air}} \frac{1}{P} \sqrt{\frac{1}{4}} = \frac{1.1\varphi I(1-\varphi)R_{air}\mu}{2\kappa_{air}P}. \end{aligned} \quad (S43)$$

Now, according to [R6], the conductivity of air can be often approximated as $\kappa_{air} = \frac{2\mu C_v'}{M} = 2\mu C_v$, where M is the molar mass of air and C_v' is the specific heat capacity at constant volume, in units of J/k mol. Thus, equation (S43) can further simplify into

$$v_{ft} = \frac{1.1\varphi I(1-\varphi)MR_{air}\mu}{4\mu C_v'} \frac{1}{P} = \frac{1.1\varphi I(1-\varphi)R_{air}}{4PC_v} = \frac{1.1\varphi(1-\varphi)R_{air}}{4C_v} \frac{I}{P} = C \frac{I}{P}. \quad (S44)$$

where the constant C is simply given by

$$C = \frac{1.1\varphi(1-\varphi)R_{air}}{4C_v} = \frac{1.1 * 0.5 * (1 - 0.5) * 0.287}{4 * 0.718} = 0.0275. \quad (S45)$$

Hence, what these series of derivations shows is that it is possible to approximate and obtain order-of-magnitude estimations of the flow-through velocity by using

$$v_{ft} = 0.0275 \frac{I}{P}. \quad (S46)$$

2.2. Lift-Force Calculations and Temperature-dependencies

Once we knew how to calculate v_{ft} and v_{out} using the equations derived above (whether it is in the simplified or full analytical form), we used the following equation to calculate the lift forces produced by each geometry, as outlined in the ANSYS simulations section at the beginning of this document:

$$\sum F = C_1 * 8 * \mu * D * v_{ft} + C_2 * \rho * A_{out} * v_{out}^2. \quad (S47)$$

Here, R is the characteristic radius of the geometry (usually the inlet radius), while μ is the viscosity and ρ the fluid density. In addition, C_1 and C_2 are the geometry dependent coefficients summarized in **Table 6**.

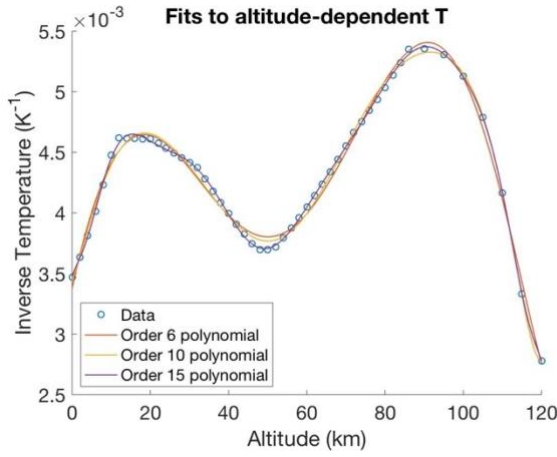
As the derivation of equations above evidences, all of the geometric (A_{total} and A_{out}) and channel (A , B , L , S , t) variables are present in (S23), meaning that it was possible to construct parametric studies exploring the dependency of v_{ft} , and consequentially lift, on all of these. Notice, all of these variables were largely independent of each other, making it possible to modify each separately. However, some other parameters within (S23), such as I_{sum} , density ρ , and air viscosity μ , were actually dependent on temperature, which in turn was also altitude dependent. As a result, in order to accurately calculate the flow-through velocities v_{ft} experienced by a 3D geometry in a range of altitudes, we needed to derive expressions for approximating the air temperature, air pressure, air viscosity and air density as a function of altitude itself.

2.2.1 Temperature-dependent Relations

We developed the relations characterizing the dependency between temperature and the fluid variable in question by using standard atmospheric⁵ empirical data and fitting equations to it. For instance, for the data describing the dependency between air temperature and altitude, we fit both a 6th, 10th and 15th order

⁵ The specific standard atmospheric data was taken from the following three websites:
https://www.engineeringtoolbox.com/standard-atmosphere-d_604.html | <https://www.pdas.com/atmosTable1SI.html>
<https://www.pdas.com/bigtables.html>

polynomial, as **Figure S12** to the below shows. Overall, the 15th order polynomial provided the best empirical fit, which was why we decided to use it for the rest of this analysis. However, one interesting aspect of this fit was that we actually fitted at the inverse of the temperature, the reason for which will become clearer in the derivation of the altitude-pressure dependency. In any case, equation (S48) below shows this explicit relation, with h (the altitude) being in kilometers, and all terms in the column added.



$$T^{-1}(h) = \begin{aligned} & -4.592 * 10^{-29} h^{15} \\ & 4.023 * 10^{-27} h^{14} \\ & 1.491 * 10^{-23} h^{13} \\ & -7.942 * 10^{-21} h^{12} \\ & 2.021 * 10^{-18} h^{11} \\ & -3.152 * 10^{-16} h^{10} \\ & 3.271 * 10^{-14} h^9 \\ & -2.332 * 10^{-12} h^8 \\ & 1.150 * 10^{-10} h^7 \\ & -3.862 * 10^{-9} h^6 \\ & 8.525 * 10^{-8} h^5 \\ & -1.150 * 10^{-6} h^4 \\ & 8.154 * 10^{-6} h^3 \\ & -2.283 * 10^{-5} h^2 \\ & 9.912 * 10^{-5} h^1 \\ & 3.473 * 10^{-3} 1. \end{aligned} \quad (S48)$$

Figure S12: Modeled temperature dependency on altitude.

Having derived the empirical relation between temperature (its inverse) and altitude, it was possible to determine a similar expression for pressure. In essence, the differential equation describing the pressure-altitude relationship is given by

$$dP(h) = -g * \rho(h) * dh, \quad (S49)$$

where g is the gravitational constant on earth, and $\rho(h)$ the density of air at a particular altitude h . Using the ideal gas law, $\rho(h)$ can be substituted to yield the following expression for the above differential in equation (S49)

$$dP(h) = -g * \frac{P(h)}{R_{air} * T(h)} * dh, \quad (S50)$$

where now R_{air} is the ideal gas constant of air and is equal to $287 \text{ J/kg} * \text{m}^3$. Easily enough, one can utilize the technique of separation of variables to obtain that

$$\frac{dP(h)}{P(h)} = \frac{-g}{R_{air} * T(h)} * dh, \quad (S51)$$

which leaves all of the pressure terms on one side, and the rest on the other. As a result, it is possible to see with more clarity why the above polynomial fit was done for the inverse of temperature. Indeed, equation (S51) can be equivalently written as

$$\frac{dP(h)}{P(h)} = \frac{-g * T^{-1}(h)}{R_{air}} * dh. \quad (S52)$$

This expression can be easily integrated to obtain the following logarithm:

$$\ln(P) = \frac{-g}{R_{air}} * \int T^{-1}(h) * dh. \quad (S53)$$

Letting $\zeta(h) = \int T^{-1}(h) * dh$ be a placeholder for the integral of the inverse temperature polynomial and C be simply a constant of integration, we obtain that

$$\ln(P(h)) = \frac{-g}{R_{air}} * \zeta(h) + C. \quad (S54)$$

Now, in order to remove the logarithm from the pressure, we can raise both sides of the expression to the Euler's number power, and get

$$P(h) = e^{\frac{-g}{R_{air}} * \zeta(h) + c} . \quad (S55)$$

After applying exponent rules, (S55) decomposes into the product given by

$$P(h) = e^c * e^{\frac{-g}{R_{air}} * \zeta(h)} , \quad (S56)$$

and can be further simplified, upon application of boundary conditions, into

$$P(h) = 101300 \text{ Pa} * e^{\frac{-g}{R_{air}} * \zeta(h)} , \quad (S57)$$

which takes the following full form:

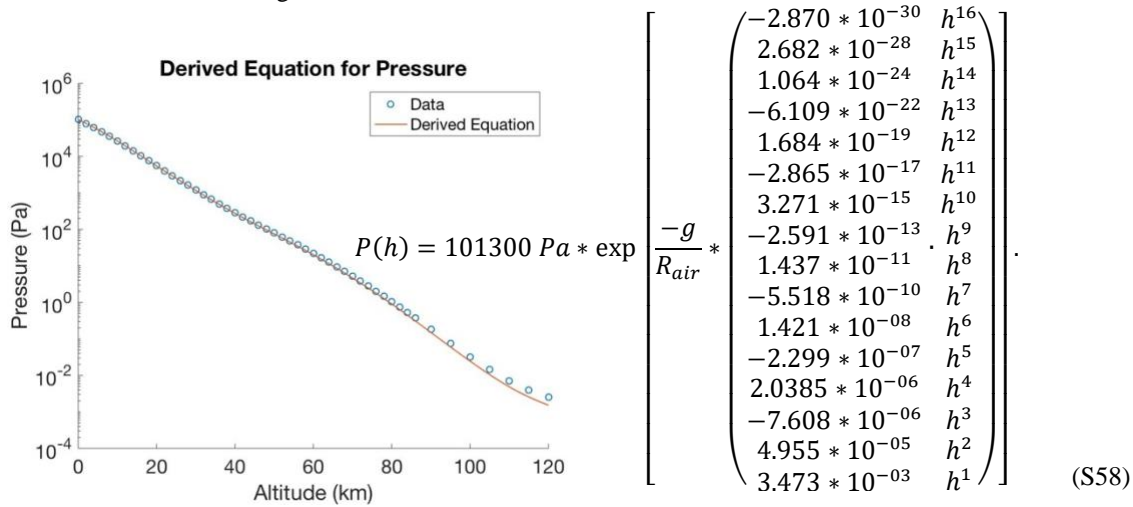


Figure S13: Modeled pressure dependency on altitude.

As **Figure S13** above shows, the agreement of this equation with the empirical data is very reasonable, especially below 80 km altitude. Above 80 km, the atmosphere is no longer well mixed, has increasing concentrations of atomic oxygen, and the simple ideal gas law we used above no longer applies. For this reason, the results that will be presented below correspond to altitudes below 80 km.

The next step was modelling the air density dependency on altitude. With expressions for $T(h)$ and $P(h)$ above, we could use the ideal gas law to write

$$\rho(h) = \frac{P(h)}{R_{air} * T(h)} . \quad (S59)$$

Finally, the last dependency that remained to be defined was the air viscosity and altitude relation. To that end, we could use Sutherland's law, which relates viscosity and temperature through the following equation:

$$\mu(h) = \mu_{ref} * \left(\frac{T(h)}{T_{ref}} \right)^{1.5} * \left(\frac{T_{ref} + S}{T(h) + S} \right) , \quad (S60)$$

where μ_{ref} is the reference dynamic viscosity and T_{ref} the reference temperature. In this work, for air, at $T_{ref} = 20 \text{ C}$, we have that $\mu_{ref} = 0.000018205 \text{ Pa} * \text{s}$. Finally, S is a constant, known as Sutherland's temperature, which is given by 110.4 K.

2.2.2 Payload Calculations

Once all of the required equations and relationships were derived, it was possible to calculate v_{ft} and v_{out} for a specific set of geometric and channel parameters defining unique 3D structures. By calculating these velocities, we determined the total force produced by each geometry, as outlined by equation (S47), from which it was possible to perform some payload estimates. However, in order to obtain the payload estimates, it was paramount to first determine the surface areas of each one of the 3D geometries in question, the reason being that density of these structure was defined in areal terms as opposed to volumetric terms. As was mentioned in the main paper, this work considered a truncated cone, truncated sphere, and a rocket, and their defining equations are shown in **Table 7** below.

Main Geometrical Area Definitions			
Area	Truncated Cone	Truncated Sphere	Rocket
A_{total}	$\pi\left(\frac{D}{2}\right)^2 + \pi\left(\frac{D}{2}\right)h_2 - \pi r(h_2 - h_1)$	$\pi(D^2 - 2rh)$	$2\pi r(r + D)$
A_{out}	πr^2		
A_{in}	φA_{total}		
A_{solid}	$(1 - \varphi)A_{total}$		
Special Variables	$h_1 = \sqrt{\left(\frac{D}{2} - r\right)^2 + D^2}$ $h_2 = \sqrt{\left(\frac{D}{2}\right)^2 + h^3}$ $h_3 = \frac{D^2}{(D - 2r)}$	$h = \left(\frac{D}{2}\right) - \sqrt{\left(\frac{D}{2}\right)^2 - r^2}$	N/A

Table 7: Area definitions used across this work for the cone, sphere and rocket. Notice that here, the variable h_3 follows from using similar triangles analysis, and letting $h_3/(D/2) = D/(D/2 - r)$. For all three geometries, the variable D represents the overall scale of the structure while r their outlet radius. Notice that A_{in} is the porous area, while A_{solid} is the solid area in which the sun's irradiance is absorbed, and it follows that $A_{total} = A_{solid} + A_{in}$.

As a result, having defined these surface areas (using the parameters established in **Figure S1**), we calculated the mass of our three 3D structures. In particular, since the cross-sectional area of a channel is simply AB , then one can define the number of channels as the following integer floor:

$$n_{channels} = \left\lfloor \frac{A_{in}}{AB} \right\rfloor. \quad (S61)$$

The number of channels, $n_{channels}$, is an important parameter, given that now it is possible to calculate the volume of the structure that is occupied by the deposited alumina around each channel, which has thickness t and relatively high density ρ_{ald} of 3950 kg/m³ [R9]. Indeed, similarly to equation (S28) above, we can define this volume as

$$V_{ald,channels} = n_{channels}(L - 2t)[(A + 2t)(B + 2t) - AB]. \quad (S62)$$

Experimentally, it has already been found that the areal density of nanocardboard, σ_{ncb} , is about 1 g/m² [R5], but this corresponds to a value of L (nanocardboard thickness) equal to 50 μ m. However, in our parametric studies, as we sweep through various values of L , especially those that are larger than 50 μ m, this areal density alone is not enough to estimate the weight of the structure. As a result, calculating the volume of alumina around each of the channels is paramount, since the structure naturally becomes heavier with increasing thickness. Hence, the overall mass of any one of these geometries will be given by

$$m_{geometry} = \sigma_{geom}(A_{solid} - A_{in}) + \rho_{ald}V_{ald,channels}, \quad (S63)$$

where this expression accounts both for the areal density (σ_{geom}) and the increases in the amount of the deposited alumina as a result of changes in the wall thickness L . Thus, the net lift produced by the geometry is simply given by subtracting the structure's weight from the force expression in (S47), or

$$Lift_{net} = F - gm_{geometry} . \quad (S64)$$

While we know from simulations what σ_{geom} is, notice that it is also possible to use our equations and a series of approximations to obtain a theoretical upper bound for this value. In essence, we can start by letting the force be equal to the expression below

$$F = \dot{m}v_{out} = (A_{in}\rho_{air}v_{ft})v_{out} = (A_{in}\frac{P}{R_{air}T}v_{ft})v_{out} , \quad (S65)$$

which incorporates mass flow rate and the ideal gas law. Now, recall that equation (S4) provides an expression relating v_{ft} and v_{out} , while (S46) provides a simplified approximation for v_{ft} . As a result, taking a conservative approach that lets $v_{out} = 0.2v_{avg}$, a fifth of the average molecular velocity of a gas, shown in (S41) above, and incorporating (S2) and (S46), it is possible to re-write (S68) to obtain

$$\begin{aligned} F &= A_{in}\frac{P}{R_{air}T}v_{ft}0.2\sqrt{\frac{8R_{air}T}{\pi}} = \\ &= 0.0055A_{in}\frac{P}{R_{air}T}\frac{I}{P}\sqrt{\frac{8R_{air}T}{\pi}} = 0.0055A_{in}\frac{I}{R_{air}T}\sqrt{\frac{8R_{air}T}{\pi}} . \end{aligned} \quad (S66)$$

Upon further simplification, equation (S69) reduces to

$$F = 0.0055A_{in}\frac{I}{R_{air}T}\sqrt{\frac{8R_{air}T}{\pi}} = 0.0055\sqrt{\frac{8}{\pi}}A_{in}I\sqrt{\frac{1}{R_{air}T}} . \quad (S67)$$

Thus, the maximum areal density that can be entertained by these 3D structures can be approximated by

$$\sigma_{geom} = \frac{F}{A_{in}g} = 0.0055\sqrt{\frac{8}{\pi}}\frac{I}{g}\sqrt{\frac{1}{R_{air}T}} = KI\sqrt{\frac{1}{R_{air}T}} = 0.016\frac{I}{v_{avg}g} , \quad (S68)$$

where $K = \frac{0.0055}{g}\sqrt{\frac{8}{\pi}} = 0.0009$ and $v_{avg} = \sqrt{8R_{air}T/\pi} \approx 400$ m/s is the average velocity of air molecules. Upon inserting the parameters, we find that σ_{geom} can have an average value of 0.004 kg/m², four times of what the areal density of nanocardboard typically is in experiments. The main paper provides additional areal density calculations based off from the parametric studies (detailed below) as well as cloud plots denoting the maximum areal density for each of the study geometries. They are generally of the same order of magnitude as the estimate (S68).

2.2.3 Parametric Studies

In this section, we provide four tables that accompany the presentation of the results shown in the main paper. In essence, **Table 8** both summarizes the chosen optimization ranges and discretization for the variables that were varied (A , L and r) and specifies the values that the remaining variables (B , N , X , S and t) took. Similarly, **Table 9** through **Table 11** present the results for the performed parametric optimization on the three geometries, detailing the specific combination of A , L and r that first, yielded the maximum payload capabilities and second, achieved flight at the lower altitude. In addition, **Table 9** through **Table 11** also provide the areal density of each structure for when the maximum payload was achieved. Notice that this process was repeated for multiple values of D , as to explore the dependency of the overall optimization results with the scale of the geometries.

Parametric Optimization Variables					
Variable	Range	Truncated Cone	Truncated Sphere	Rocket	Discretization
A	Min.	10 mm			80 equally spaced points (log scale)
	Max.	5 mm			
L	Min.	1 μ m			80 equally spaced points

	Max.	1 cm	(log scale)
r	Min.	$r_{\min} = D/20$ (see Table 9 through Table 12)	80 equally spaced points (log scale)
	Max.	$r_{\max} = D/2.01$ (see Table 9 through Table 12)	
Altitude	Min.	0 km	17 equally spaced points (5 km intervals)
	Max.	80 km	
B		$10A$	
N		1 sun	
X		$\frac{B - S}{S + A}$	
S		A	
t		50 nm	

Table 8: Main values used across the various variables during the parametric optimization. As can be seen, the search range for the optimal A , L and r was discretized in all three cases in 100 points, following a log scale. Changing the granularity of the discretization or the bounds of the search range did not significantly modify the results seen in **Table 9** through **Table 11** below.

Parametric Optimization Results – Various Sphere Sizes							
Variable	Case	$D = 2$ cm	$D = 0.1$ m	$D = 0.5$ m	$D = 1$ m	$D = 2$ m	$D = 5$ m
		$r_{\min} = D/20, r_{\max} = D/2.01$, with a discretization of 80 points (log scale)					
A	Max. Payload	0.90 mm	0.90 mm	0.90 mm	0.90 mm	0.90 mm	0.90 mm
	Min. Altitude	0.13 mm	0.13 mm	0.20 mm	0.20 mm	0.20 mm	0.20 mm
L	Max. Payload	0.91 mm	0.91 mm	0.91 mm	0.91 mm	0.91 mm	0.91 mm
	Min. Altitude	0.14 mm	0.14 mm	0.21 mm	0.21 mm	0.21 mm	0.21 mm
r	Max. Payload	9.95 mm	4.07 cm	19.05 cm	36.85 cm	73.70 cm	1.84 m
	Min. Altitude	4.05 mm	1.89 cm	10.82 cm	21.63 cm	43.27 cm	1.08 m
Max. Payload	Payload (mg)	8.34	79.11	1 445	5 526	21 612	133 242
	Altitude (km)	80	80	80	80	80	80
	A. Density (g/m ²)	25.48	7.81	5.91	5.64	5.54	5.49
	Sphere Area (m ²)	0.0007	0.025	0.64	2.63	10.52	65.82
	A_{total}/A_{out} ratio	2.22	4.77	5.68	6.17	6.17	6.17
Min. Altitude	Payload (mg)	0.24	0.58	223.94	872.33	3 442	21 339
	Altitude (km)	55	55	60	60	60	60
	A_{total}/A_{out} ratio	23.34	26.96	20.30	20.32	20.31	20.38

Table 9: Combinations of A , L and r that returned the spheres capable of carrying the greatest payload and achieving flight at the lowest altitude, for various values of D , as specified in **Figure S1**.

Parametric Optimization Results – Various Cone Sizes							
Variable	Case	$D = 2$ cm	$D = 0.1$ m	$D = 0.5$ m	$D = 1$ m	$D = 2$ m	$D = 5$ m
		$r_{\min} = D/20, r_{\max} = D/2.01$, with a discretization of 80 points (log scale)					
A	Max. Payload	0.90 mm	0.90 mm	0.90 mm	0.90 mm	0.90 mm	0.90 mm
	Min. Altitude	0.13 mm	0.35 mm	0.35 mm	0.35 mm	0.35 mm	0.35 mm
L	Max. Payload	0.91 mm	0.91 mm	0.91 mm	0.91 mm	0.91 mm	0.91 mm
	Min. Altitude	0.14 mm	0.36 mm	0.36 mm	0.36 mm	0.36 mm	0.36 mm
r	Max. Payload	9.95 mm	4.97 cm	24.86 cm	49.73 cm	99.45 cm	2.49 m
	Min. Altitude	4.05 mm	2.39 cm	11.56 cm	23.12 cm	46.25 cm	1.16 m
Max. Payload	Payload (mg)	7.96	101.26	2 043	7 929	31 228	193 348
	Altitude (km)	80	80	80	80	80	80
	A. Density (g/m ²)	11.59	6.61	5.61	5.48	5.42	5.38
	Cone Area (m ²)	0.0016	0.039	0.98	3.92	15.67	97.97
	A_{total}/A_{out} ratio	5.04	5.05	5.05	5.04	5.04	5.03
Min. Altitude	Payload (mg)	0.18	10.12	208.65	812.97	3 209	19 892
	Altitude (km)	55	60	60	60	60	60
	A_{total}/A_{out} ratio	23.97	17.75	18.84	18.84	18.83	18.72

Table 10: Combinations of A , L and r that returned the cones capable of carrying the greatest payload and achieving flight at the lowest altitude, for various values of D , as specified in **Figure S1**.

Parametric Optimization Results – Various Rocket Sizes							
Variable	Case	D = 2 cm	D = 10 cm	D = 0.5 m	D = 1 m	D = 2 m	D = 5 m
		$r_{min} = D/20, r_{max} = D/2.01$, with a discretization of 80 points (log scale)					
A	Max. Payload	0.90 mm	0.90 mm	0.90 mm	0.90 mm	0.90 mm	0.90 mm
	Min. Altitude	0.092 mm	0.13 mm	0.13 mm	0.13 mm	0.13 mm	0.13 mm
L	Max. Payload	0.91 mm	0.91 mm	0.91 mm	0.91 mm	0.91 mm	0.91 mm
	Min. Altitude	0.094 mm	0.14 mm	0.14 mm	0.14 mm	0.14 mm	0.14 mm
r	Max. Payload	9.95 mm	4.97 cm	24.86 cm	49.73 cm	99.45 cm	2.49 m
	Min. Altitude	1.00 mm	0.94 cm	4.12 cm	8.24 cm	15.94 cm	0.40 m
Max. Payload	Payload (mg)	9.51	127.59	2 639	10 281	40 573	251 516
	Altitude (km)	80	80	80	80	80	80
	A. Density (g/m ²)	11.60	6.89	5.95	5.83	5.77	5.74
	Rocket Area (m ²)	0.0019	0.047	1.17	4.68	18.71	117.12
	A_{total}/A_{out} ratio	6.02	6.02	6.02	6.02	6.02	6.02
Min. Altitude	Payload (mg)	0.03	1.54	8.29	18.57	45.37	175.67
	Altitude (km)	45	55	55	55	55	55
	A_{total}/A_{out} ratio	42	23.28	26.27	26.27	27.09	27

Table 11: Combinations of A, L and r that returned the rockets capable of carrying the greatest payload and achieving flight at the lowest altitude, for various values of D, as specified in **Figure S1**.

The results from these tables are discussed in greater detail in the main paper. However, there are four important points to highlight. First, changing D (the scaling of the overall geometries) did not affect significantly the optimal channel parameters A and L that yielded the maximum payload capabilities and achieved flight at the lowest altitude. Secondly, the obtained maximum areal densities were similar across the three geometries (as seen in **Figure S14 (a)** below) and had average values of 9.31 g/m², 6.68 g/m² and 6.96 g/m², for the sphere, cone, and rocket, respectively. Notice that these are above the theoretical order-of-magnitude estimation for the upper limit of 4 g/m² in (S71). Thirdly, the optimized A_{total}/A_{out} ratios for the three geometries were relatively invariant across the various values of D and the two missions (max. payload and minimum altitude). For instance, for the maximum payload optimization, A_{total}/A_{out} averaged 5.20, 5.04, and 6.02 for the sphere, cone and rocket, respectively, while for the minimum altitude case, this ratio averaged 21.94, 19.49 and 28.65, respectively. Lastly, for a given surface area, the amount of payload that each geometry could carry was comparable, as can be seen in **Figure S14 (b)** below. As a result, 1 m² of a porous and geometrically optimized cone has a similar maximum payload capability than 1 m² of an optimized rocket and sphere.

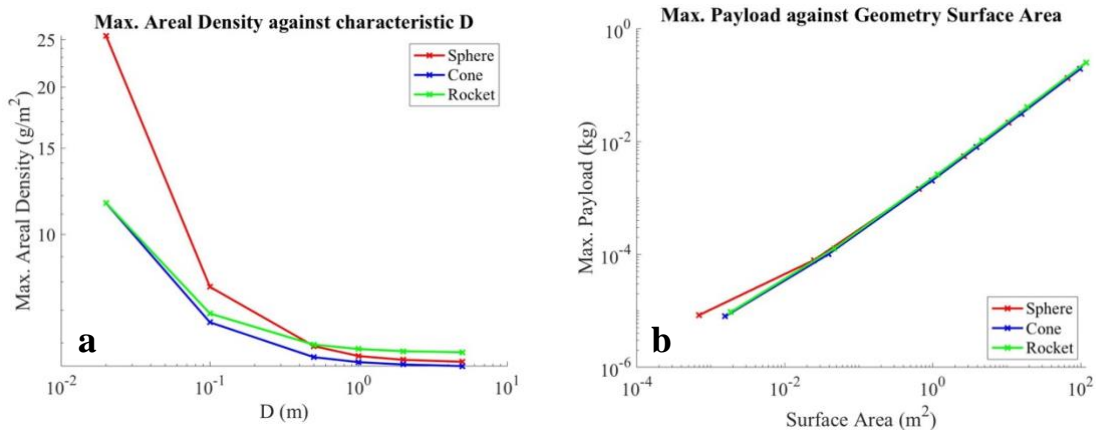


Figure S14: D against Areal Density (a) and Surface Area against Payload (b) for the 3D geometries.

Finally, **Figure S15** through **Figure S20** present cloud plots that permit visualizing the results from the parametric studies, in particular how different combinations of A , L and r enabled geometries with various altitude (a), payload (b) and areal density (c) capabilities. These plots correspond to the $D = 10$ cm and $D = 10$ m cone, sphere and rocket, and are accompanied with illustrations of the optimized geometries that achieved flight at minimum altitude (d) and carried the most payload (e). These figures were generated by discretizing the search ranges of A , L and r in 500 equally spaced, and the results from the optimized geometries are shown in Table 12 through Table 14). Despite the increase in discretization points (from 80 to 500) in each dimension, the results were comparable.

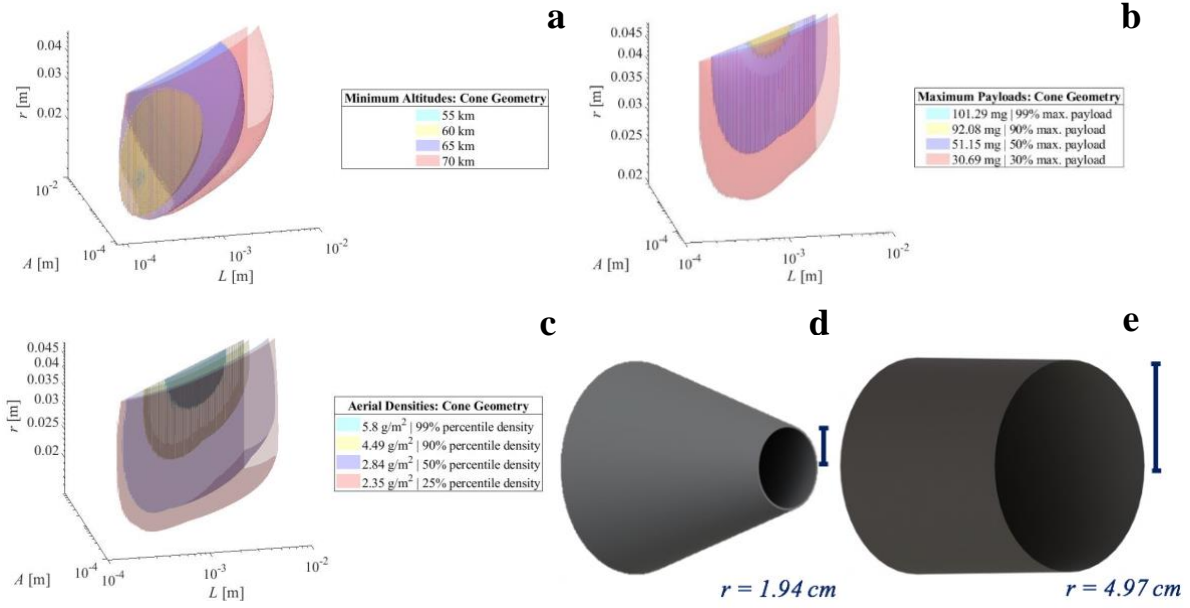


Figure S15: Minimum Altitude (a), Maximum Payload (b) and Areal Density (c) plots for the $D = 10$ cm Cone Geometry. Here, the geometry that was able to levitate payload at minimum altitude (0.52 mg at 55 km) is shown in (d), while that which was able to levitate the maximum payload (102.31 mg at 80 km) is shown in (e).

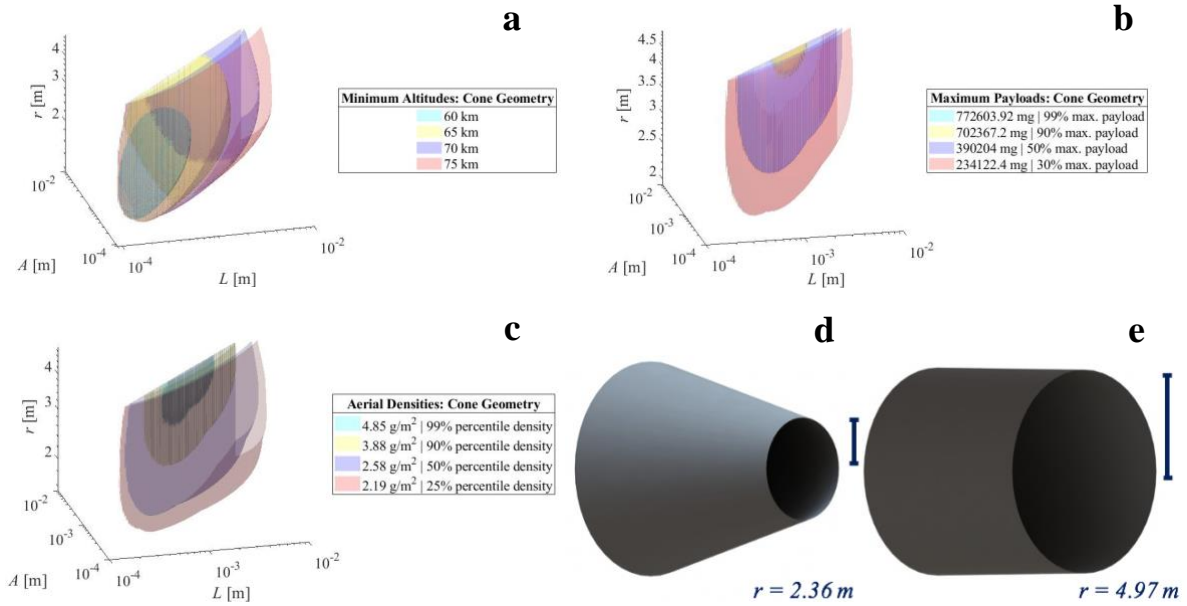


Figure S16: Minimum Altitude (a), Maximum Payload (b) and Areal Density (c) plots for the $D = 10$ m Cone Geometry. Here, the geometry that was able to levitate payload at minimum altitude (95 288 mg at 60 km) is shown in (d), while that which was able to levitate the maximum payload (780 408 mg at 80 km) is shown in (e).

Comparison of $D = 10$ cm and $D = 10$ m Cone Geometries								
Case		A	L	r	Surface Area (m ²)	A_{total}/A_{out} ratio	Payload (mg)	Altitude (km)
		Discretization of 500 points						
D = 10 cm	Min. Altitude	0.15 mm	0.16 mm	1.94 cm	0.03	25.92	0.52	55
	Max. Payload	1.24 mm	1.25 mm	4.97 cm	0.04	5.05	102.31	80
D = 10 m	Min. Altitude	0.21 mm	0.22 mm	2.36 m	317.52	18.16	95 288	60
	Max. Payload	1.24 mm	1.25 mm	4.97 m	391.56	5.05	780 408	80

Table 12: Combinations of A , L and r that returned the optimal cone geometries described in **Figure S15** and **Figure S16** above.

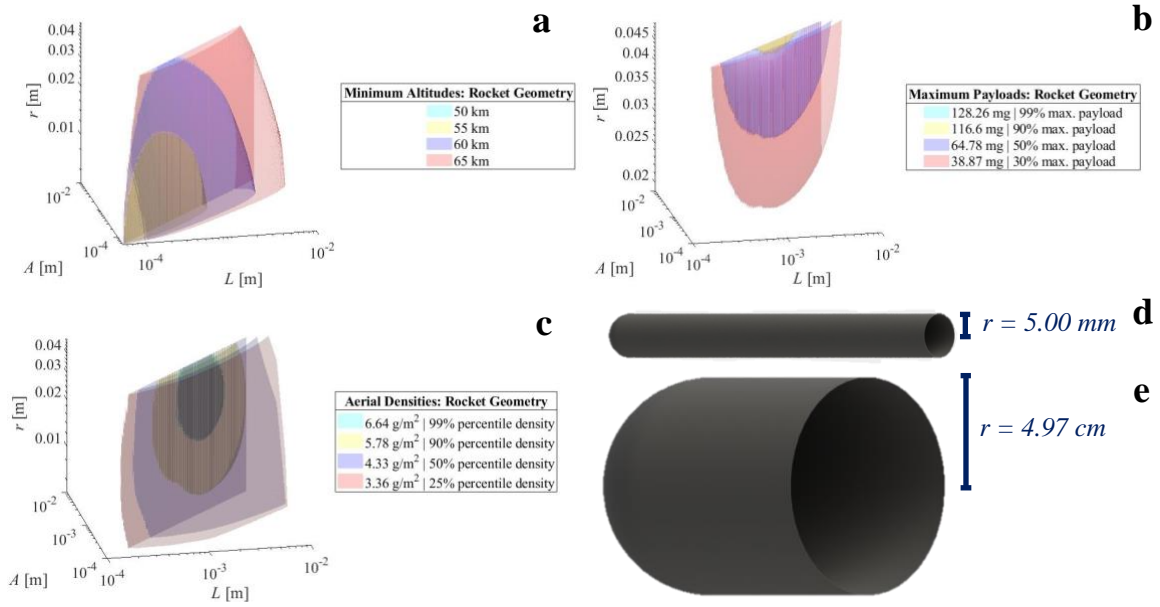


Figure S17: Minimum Altitude (a), Maximum Payload (b) and Areal Density (c) plots for the $D = 10$ cm Rocket Geometry. Here, the geometry that was able to levitate payload at minimum altitude (0.01 mg at 50 km) is shown in (d), while that which was able to levitate the maximum payload (129.56 mg at 80 km) is shown in (e).

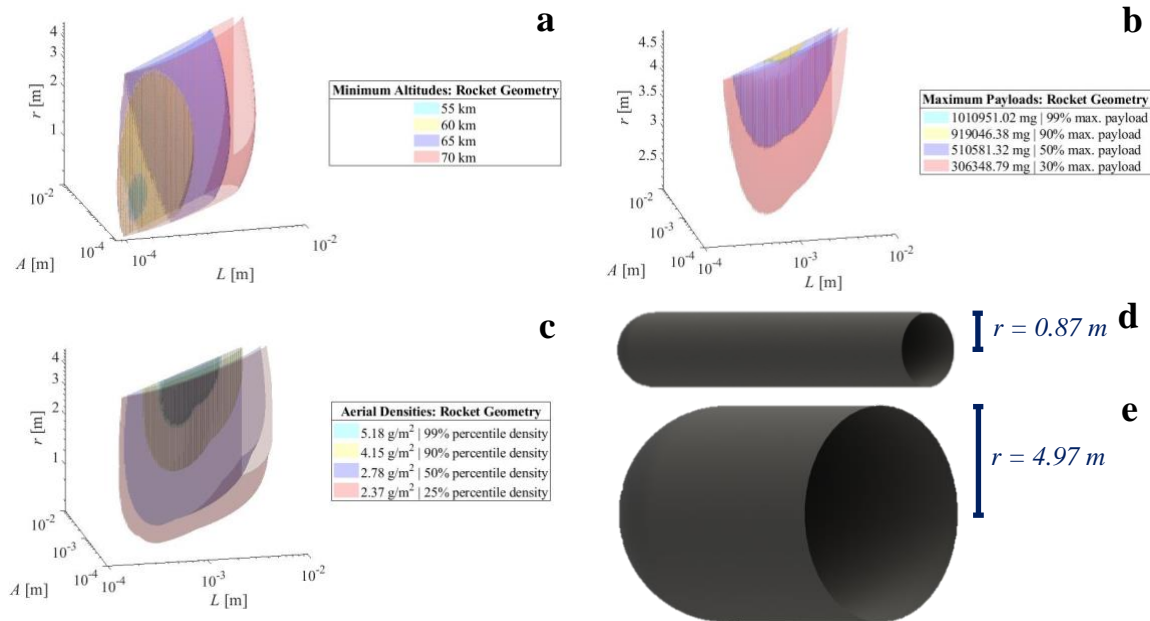


Figure S18: Minimum Altitude (a), Maximum Payload (b) and Areal Density (c) plots for the $D = 10$ m Rocket Geometry. Here, the geometry that was able to levitate payload at minimum altitude (2 132.57 mg at 55 km) is shown in (d), while that which was able to levitate the maximum payload (1 021 162 mg at 80 km) is shown in (e).

Comparison of $D = 10$ cm and $D = 10$ m Rocket Geometries								
Case	A	L	r	Surface Area (m ²)	A_{total}/A_{out} ratio	Payload (mg)	Altitude (km)	
	Discretization of 500 points							
D = 10 cm	Min. Altitude	0.11 mm	0.12 mm	0.50 cm	0.001	>100	0.01	50
	Max. Payload	1.24 mm	1.25 mm	4.97 cm	0.05	6.02	129.56	80
D = 10 m	Min. Altitude	0.15 mm	0.16 mm	0.87 m	59.39	24.98	2132.57	55
	Max. Payload	1.24 mm	1.25 mm	4.97 m	467.23	6.02	1021162	80

Table 13: Combinations of A , L and r that returned the optimal rocket geometries described in **Figure S17** and **Figure S18** above.

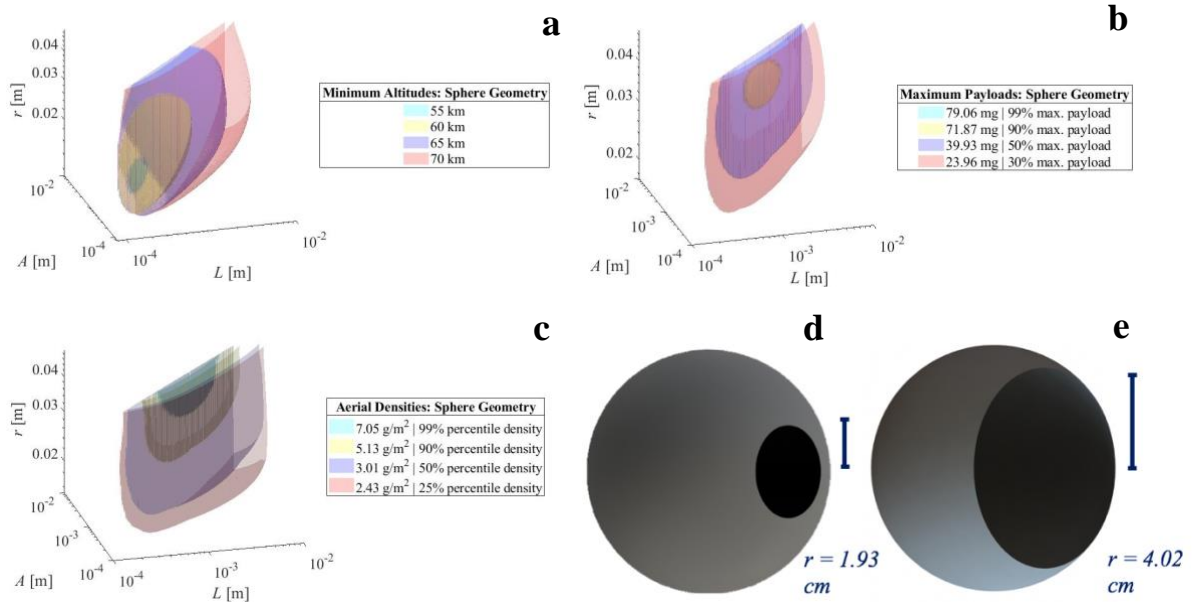


Figure S19: Minimum Altitude (a), Maximum Payload (b) and Areal Density (c) plots for the $D = 10$ cm Sphere Geometry. Here, the geometry that was able to levitate payload at minimum altitude (1.41 mg at 55 km) is shown in (d), while that which was able to levitate the maximum payload (79.86 mg at 80 km) is shown in (e).

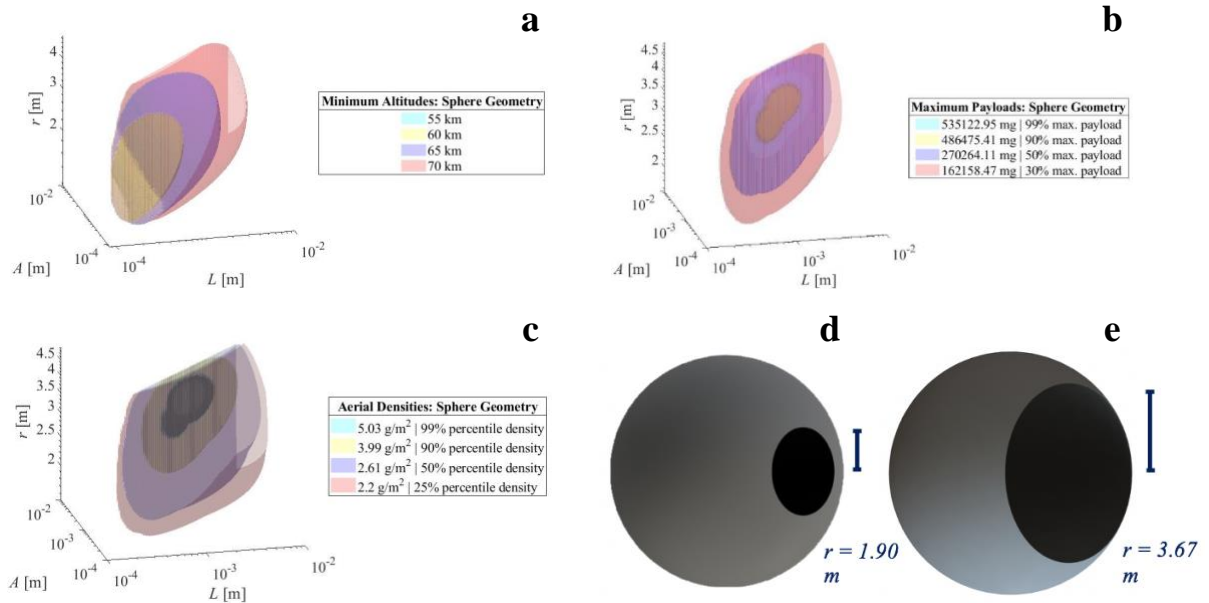


Figure S20: Minimum Altitude (a), Maximum Payload (b) and Areal Density (c) plots for the $D = 10$ m Sphere Geometry. Here, the geometry that was able to levitate payload at minimum altitude (831.92 mg at 55 km) is shown in (d), while that which was able to levitate the maximum payload (540 528 mg at 80 km) is shown in (e).

Comparison of $D = 10$ cm and $D = 10$ m Sphere Geometries								
Case		A	L	r	Surface Area (m ²)	A_{total}/A_{out} ratio	Payload (mg)	Altitude (km)
		Discretization of 500 points						
D = 10 cm	Min. Altitude	0.15 mm	0.16 mm	1.93 cm	0.03	25.81	1.41	55
	Max. Payload	1.03 mm	1.04 mm	4.02 cm	0.03	4.93	79.86	80
D = 10 m	Min. Altitude	0.15 mm	0.16 mm	1.90 m	302.22	26.66	831.92	55
	Max. Payload	1.24 mm	1.25 mm	3.67 m	263.63	6.23	540 528	80

Table 14: Combinations of A , L and r that returned the optimal sphere geometries described in **Figure S19** and **Figure S20** above.

References

- [R1] Azadi, Mohsen, George A. Popov, Zhipeng Lu, Andy G. Eskenazi, Avery Ji Won Bang, Matthew F. Campbell, Howard Hu, and Igor Bargatin. "Controlled levitation of nanostructured thin films for sun-powered near-space flight." *Science Advances* 7, no. 7 (2021): eabe1127.
- [R2] Cappella, Andrea, Jean-Luc Battaglia, Vincent Schick, Andrzej Kusiak, Alessio Lamperti, Claudia Wiemer, and Bruno Hay. "High Temperature Thermal Conductivity of Amorphous Al₂O₃ Thin Films Grown by Low Temperature ALD." *Advanced Engineering Materials* 15, no. 11 (2013): 1046-1050.
- [R3] Cortes, John, Christopher Stanczak, Mohsen Azadi, Maanav Narula, Samuel M. Nicaise, Howard Hu, and Igor Bargatin. "Photophoretic levitation of macroscopic nanocardboard plates." *Advanced Materials* 32, no. 16 (2020): 1906878.
- [R4] Eskenazi, Andy, Tom Celenza, and Igor Bargatin. "MATLAB-fluid-flow-parametric-studies." (2022) <https://github.com/andyeske/MATLAB-fluidflow-parametric-studies>
- [R5] Lin, Chen, Samuel M. Nicaise, Drew E. Lilley, Joan Cortes, Pengcheng Jiao, Jaspreet Singh, Mohsen Azadi et al. "Nanocardboard as a nanoscale analog of hollow sandwich plates." *Nature communications* 9, no. 1 (2018): 1-8.
- [R6] O'Neal Jr, Cleveland, and Richard S. Brokaw. "Relation between thermal conductivity and viscosity for some nonpolar gases." *The Physics of Fluids* 5, no. 5 (1962): 567-574.
- [R7] Sharipov, Felix, and Vladimir Seleznev. "Data on internal rarefied gas flows." *Journal of Physical and Chemical Reference Data* 27, no. 3 (1998): 657-706.
- [R8] Teagan, William P., and George S. Springer. "Heat-Transfer and Density-Distribution Measurements between Parallel Plates in the Transition Regime." *The Physics of Fluids* 11, no. 3 (1968): 497-506.
- [R9] Wagiman, Abdullah, Mohammad Sukri Mustapa, Mohd Amri Lajis, Shazarel Shamsudin, Mahmud Abd Hakim, and Rosli Asmawi. "Effect of Thermally Formed Alumina on Density of AlMgSi Alloys Extrudate Recycled Via Solid State Technique." *Journal of Advanced Research in Fluid Mechanics and Thermal Sciences* 87, no. 2 (2021): 137-144.
- [R10] Wu, H., S. Grabarnik, A. Emadi, G. De Graaf, and R. F. Wolffenbuttel. "Characterization of thermal cross-talk in a MEMS-based thermopile detector array." *Journal of Micromechanics and Microengineering* 19, no. 7 (2009): 074022.